Pergamon

Geochimica et Cosmochimica Acta, Vol. 68, No. 6, pp. 1413–1431, 2004

0016-7037/04 $30.00 + .00

doi:10.1016/j.gca.2003.09.017

Pt-Re-Os systematics of group IIAB and IIIAB iron meteorites

D. L. Cook,[1,*] R. J. Walker,[1,†] M. F. Horan,[2] J. T. Wasson,[3] and J. W. Morgan[1,‡]

[1]Isotope Geochemistry Laboratory, Department of Geology, University of Maryland, College Park, MD 20742, USA
[2]Department of Terrestrial Magnetism, Carnegie Institution of Washington, 5241 Broad Branch Road NW, Washington, DC 20015, USA
[3]Institute of Geophysics and Planetary Physics, University of California, Los Angeles, CA 90095-1567, USA

(*Received February* 13, 2003; *accepted in revised form September* 24, 2003)

Abstract—The Pt-Re-Os isotopic and elemental systematics of 13 group IIAB and 23 group IIIAB iron meteorites are examined. As has been noted previously for iron meteorite groups and experimental systems, solid metal–liquid metal bulk distribution coefficients (D values) for both IIAB and IIIAB systems show $D_{Os}>D_{Re}>>D_{Pt}>1$ during the initial stages of core crystallization. Assuming closed-system crystallization, the latter stages of crystallization for each core are generally characterized by $D_{Pt}>D_{Re}>D_{Os}$. The processes governing the concentrations of these elements are much more complex in the IIIAB core relative to the IIAB core. Several crystallization models utilizing different starting parameters and bulk distribution coefficients are considered for the Re-Os pair. Each model has flaws, but in general, the results suggest that the concentrations of these elements were dominated by equilibrium crystallization and subsequent interactions between solid metal and both equilibrium and evolved melts. Late additions of primitive metal to either core were likely minor or nonexistent.

The ^{187}Re-^{187}Os systematics of the IIAB and IIIAB groups are consistent with generally closed-system behavior for both elements since the first several tens of Ma of the formation of the solar system, consistent with short-lived chronometers. The Re-Os isochron ages for the complete suites of IIAB and IIIAB irons are 4530 ± 50 Ma and 4517 ± 32 Ma, respectively, and are similar to previously reported Re-Os ages for the lower-Ni endmembers of these two groups. Both isochrons are consistent with, but do not require crystallization of the entire groups within 10–30 Ma of the initiation of crystallization.

The first high-precision ^{190}Pt-^{186}Os isochrons for IIAB and IIIAB irons are presented. The Pt-Os isochron ages for the IIAB and IIIAB irons, calculated using the current best estimate of the λ for ^{190}Pt, are 4323 ± 80 Ma and 4325 ± 26 Ma respectively. The Re-Os and Pt-Os ages do not overlap within the uncertainties. The younger apparent ages recorded by the Pt-Os system likely reflect error in the ^{190}Pt decay constant. The slope from the Pt-Os isochron is combined with the age from the Re-Os isochron for the IIIAB irons to calculate a revised λ of 1.415×10^{-12} a^{-1} for ^{190}Pt, although additional study of this decay constant is still needed.

1. INTRODUCTION

Iron meteorites are pieces of Fe-Ni metal that segregated from chondritic silicates during the early stages of solar system evolution. Most iron meteorites fall into one of about 13 groups and are classified on the basis of their structures and trace element contents (Wasson, 1974; Buchwald, 1975; Wasson and Kallemeyn, 2002). Each group presumably formed in a distinct parent body (Kelly and Larimer, 1977). Iron meteorites belonging to 10 of the 13 groups most likely represent the cores of different parent bodies and are known as "magmatic irons" (Wasson, 1974). The other groups are termed "nonmagmatic irons" and likely derive from parent bodies in an arrested state of differentiation and do not represent core materials (Wasson and Wang, 1986; Choi et al., 1995; Stewart et al., 1996; Wasson and Kallemeyn, 2002). Here we examine the Pt-Re-Os elemental and isotopic systematics of the two largest magmatic iron groups, IIAB and IIIAB. Utilizing the distributions of these elements, the ratios of solid metal–liquid metal bulk distribution coefficients (D values) are determined. Rhenium and Os D values for both high- and low-S systems are combined with two sets of starting compositions to model crystal–liquid fractionation processes potentially involved in the generation of the IIIAB iron system. Finally, the ^{187}Re-^{187}Os and ^{190}Pt-^{186}Os isotopic systematics of these meteorites are examined to constrain the duration of their crystallization.

Constraining the timing of late-stage crystallization is essential for understanding the complete cooling histories of the parent bodies of iron meteorites. Tungsten isotope compositions indicate that the metal comprising at least some iron meteorite groups segregated from silicates within ~0–20 Ma of solar system formation (Harper and Jacobsen, 1996; Lee and Halliday, 1996; Horan et al., 1998; Schoenberg et al., 2002). Because of the essentially complete isolation of W from Hf during core formation, this system cannot be used to determine metal-crystallization ages. The long-lived Re-Os system, coupled with the short-lived Pd-Ag and Mn-Cr systems, suggest that the cores of iron meteorite parent bodies began to crystallize within the first 40 Ma (Luck et al., 1980; Smoliar et al., 1996; Shen et al., 1996; Chen and Wasserburg, 1996; Birck and Allègre, 1998; Carlson and Hauri, 2001; Chen et al., 2002). The duration of core crystallization, however, remains poorly constrained for the larger, more complex cores. It is plausible that crystallization of group IIAB and IIIAB irons may have occurred over tens of Ma because crystal–liquid fractionation led

* Author to whom correspondence should be addressed (rjwalker@geol.umd.edu).
† *Present address:* Department of the Geophysical Sciences, University of Chicago, 5734 S. Ellis Avenue, Chicago, IL 60637.
‡ *Present address:* 510 S. Rose Avenue, Bloomington, IN 47401

to increases in the S and P contents of fractionated melts. This, in turn, would have led to large decreases in liquidus temperatures and long crystallization periods, especially for insulated pockets of trapped liquid (Wasson, 1999).

Crystal–liquid fractionation of metallic magmas typically produces large variations in Re/Os and Pt/Os ratios during core solidification, making both isotope systems viable for isochron chronometry (Hirt et al., 1963; Luck et al., 1980; Pernicka and Wasson, 1987). Extensive crystal–liquid fractionation of IIAB and IIIAB cores produced decreases of several orders of magnitude in the concentrations of Re and Os, but only modest decreases in Pt concentrations, leading to much larger variations in Pt/Os relative to Re/Os for both groups. Despite this advantage for isochron dating, the Pt-Os system is not without shortcomings relative to the Re-Os system. The long half-life (ca. 470 b.y.) of ^{190}Pt coupled with its miniscule isotopic abundance (0.01292 atomic %; Morgan et al., 2002) has produced only modest enrichments of radiogenic ^{186}Os in most geologic materials and a correspondingly narrow range in ^{186}Os/^{188}Os ratios. In general, these variations are much less than those of ^{187}Os/^{188}Os ratios produced by the decay of ^{187}Re. Thus, the detection and resolution of variations in ^{186}Os/^{188}Os ratios requires that the precision of the measurements exceed those of ^{187}Os/^{188}Os by at least an order of magnitude (Walker et al., 1997).

2. ANALYTICAL METHODS

2.1. Sample Preparation and Chemical Processing

Iron meteorite samples were cut into appropriately sized, rectangular pieces using a Leco Vari-cut saw with a 5.0-inch-diameter diamond wafering blade. The saw's cooling system was modified to use high-purity water rather than oil. To avoid cross-contamination between samples, the blade and blade assembly were cleaned with water after each sample was cut, and the cooling water was discarded and replaced. Blades were further cleaned by cutting a piece of carborundum after washing the blade and before cutting the next sample. Three separate blades were dedicated to cutting low-abundance (<100 ppb Os), intermediate-abundance (100 to 1000 ppb Os), and high-abundance (>1000 ppb Os) samples. Also, samples were cut in ascending order of Os concentration. Before dissolution, each piece was mechanically cleaned by polishing with carborundum. A separate piece of carborundum was used for each sample. Polished pieces were examined under a binocular microscope to verify cleanliness.

Samples were dissolved using the Carius tube technique described by Shirey and Walker (1995). The meteorite samples were dissolved at 200°C over a 24- to 48-h period. Two different sized tubes were used for the dissolution procedure. High-abundance meteorite samples were dissolved in small (21-cc) borosilicate Carius tubes. Low-abundance meteorite samples were dissolved in large (100-cc) tubes. Intermediate-abundance meteorite samples were dissolved in either small or large-sized Carius tubes, depending on the sample weight. The use of larger Carius tubes allows for the liberation of larger quantities of Re and Os for analysis. Meteorite sample weights ranged from 0.060 to 2.3 g. The maximum sample weight dissolved in a small Carius tube was 0.55 g. Samples were dissolved using reverse aqua regia (2:1 conc. HNO_3 to conc. HCl) to ensure complete sample digestion and equilibration between the sample and spike. Samples placed into small Carius tubes were dissolved in 7.5 g of reverse aqua regia. For samples placed into large Carius tubes, the quantity of reverse aqua regia was scaled for the sample size and ranged between 35 and 40 g. The acids used were quartz-distilled twice and Teflon-distilled once to reduce chemical blanks.

After sample dissolution, the Os was recovered from the aqua regia solution via solvent extraction using CCl_4 (Cohen and Waters, 1996), and the Os fractions were further purified via micro-distillation (Roy-Barman and Allègre, 1994). The Re and Pt were recovered via anion-exchange chromatography. The columns were packed with approximately 2.5 mL of AG1X8 anion resin (100–200 mesh). The Re was eluted with 10 mL 5–6 mol/L HNO_3. The Pt was eluted by adding an additional 10 mL of concentrated HNO_3 to the column. The Re fraction was passed through a second column packed with 0.25 mL of the same resin and eluted with 4 mL of 6 mol/L HNO_3.

Purified Os and Re were loaded onto Pt ribbon filaments for analysis. To do this, Os was redissolved in concentrated, Teflon-distilled HBr, and 1.0 μL of solution was then loaded onto the filament and dried at 1.0 A in air. Approximately 0.1 μL of a $Ba(OH)_2$ solution was then loaded onto the filament and dried at 1.0 A in air. Rhenium was redissolved in concentrated HNO_3. Two methods for loading Re were employed. The first method consisted of loading 1.0 μL of redissolved Re solution onto the filament, drying at 0.5 A in air, adding approximately 0.5 μL of the $Ba(OH)_2$ solution, and drying again at 0.5 A in air. The current to the filament was then slowly increased to approximately 1.5 A. This additional heating of the filament caused organic contaminants to be burned off of the filament, which improved signal strength and stability during the analysis; this method was used from December 1999 to December 2001. The second method consisted of mixing 1.0 μL of Re solution with 0.7 μL of a $Ba(NO_3)_2$ solution. The mixture was then added to the filament and dried at 0.5 A in air. This method was used from January 2001 to April 2001. The second method resulted in much greater signal strengths (up to two orders of magnitude) for a given quantity of Re. The second method was used for the analysis of all samples with low concentrations of Re.

The concentrations of Os and Re were determined via isotope dilution, using a mixed Re-Os spike enriched in ^{190}Os and ^{185}Re. The Os concentration measurements were made using a Sector 54 multi-collector solid source mass spectrometer at the University of Maryland, College Park. The meteorite analyses were done in static, multi-collector Faraday cup mode. The 2σ external reproducibility for approximately 35 ng aliquants of an Os standard was $\pm$0.026% and $\pm$0.010% for ^{187}Os/^{188}Os and ^{186}Os/^{188}Os, respectively (n = 16). These data were collected with signal strength of approximately 1.0 V on mass 240 (^{192}Os^{16}O$_3$).

The Re concentration and the Re and Os blank measurements were all made using a National Bureau of Standards, 30 cm radius of curvature, 68° sector, single collector mass spectrometer at the University of Maryland, College Park. The Re concentration analyses were accomplished using a Faraday cup, and the blanks were measured using an electron multiplier. The temperature of the filament was monitored during the Re concentration analyses using an optical pyrometer, and the data were collected at filament temperatures ranging between 855 and 870°C. This was done to ensure similar run conditions for all samples and to minimize fractionation effects and contamination by natural Re contained in the Pt filament. The 2σ external reproducibility for ^{185}Re/^{187}Re for loadings of approximately 1 ng of a Re standard was $\pm$0.13% (n = 9).

The Pt concentrations were determined via isotope dilution, using a Pt spike enriched in ^{198}Pt. The Pt concentration measurements were performed using a Plasma 54 multi-collector inductively coupled plasma mass spectrometer (ICP-MS) at the Carnegie Institute of Washington, Washington, D.C. Sample analyses were made in static, Faraday cup mode, and Pt blanks were measured using an electron multiplier. Mass fractionation was corrected using an exponential law and ^{194}Pt/^{195}Pt $\equiv$ 0.9744. Sample analyses were interspersed with standard analyses to monitor data quality. The in-run variations for the measurement of ^{198}Pt/^{195}Pt of all samples were less than $\pm$0.1% (2σ).

2.2. Chemical Blanks

The establishment of low, reproducible Re blanks is critical for obtaining high-precision data for the higher-Ni IIAB and IIIAB irons which have low Re concentrations. From December 1999 to December 2000, Re blanks averaged 18 and 25 pg for large and small size Carius tubes, respectively. The difference likely reflects a greater contribution of Re from the borosilicate glass used in the construction of the smaller tubes.

Filament loading blanks, resulting from Re contained in the ribbon that was used for the mass spectrometric analyses, were investigated in July 2000. Two brands of Pt ribbon and one brand of Ni ribbon were analyzed. ESPI brand Pt ribbon provided the lowest Re blank (0.54 pg),

and H Cross Co. brand Pt ribbon provided the highest Re blank (26.4 pg). ESPI brand Pt ribbon was used for all Re analyses beginning in August 2000. With improvements to reagent distillation and filament loading techniques, all Re blanks measured between January and April 2001 were below 7.0 pg, with average values of 4.8 and 4.0 pg for large and small size Carius tubes, respectively. For all low-Re abundance samples (<8 ppb), data are reported only for samples that were processed after the major improvements in the Re blank were achieved.

Initial Os blanks averaged 17 and 18 pg for the large and small size Carius tubes, respectively. The Pt blanks averaged 2100 and 9700 pg for the large and small size Carius tubes, respectively. After improvements to reagent distillation, the Os blanks averaged 10 and 12 pg for the large and small size Carius tubes, respectively, and the Pt blanks averaged 330 and 920 pg for the large and small size Carius tubes, respectively. As with the Re blanks, the difference likely reflects the purity of the borosilicate glass used in the construction of the tubes. For most samples, Os and Pt blanks were negligible (<0.1%).

2.3. $^{186}Os/^{188}Os$ Data Calibration

A small increase in measured $^{186}Os/^{188}Os$ ratios for spiked standards was noted. To calibrate this effect, seven standard-spike mixes were prepared with $^{190}Os/^{192}Os$ ratios ranging from 0.86 to 2.1. The measured $^{186}Os/^{188}Os$ ratios of each mixture were compared to the average value of the unspiked standard to determine the amount of deviation caused by the addition of the spike. The deviation of the spiked $^{186}Os/^{188}Os$ ratios from the average, unspiked standard value is positively correlated with the amount of spike added. The best-fit line has a slope of 0.0000186 and an $r^2 = 0.79$. This relationship provides the following correction:

$$^{186}Os/^{188}Os_{corrected} = {}^{186}Os/^{188}Os_{measured} - [(0.0000186 \times {}^{190}Os/^{192}Os) - 0.0000011)]$$

The $^{186}Os/^{188}Os$ data have also been corrected for bias introduced during analyses conducted in the static, multi-collector Faraday cup mode. The average standard value for $^{186}Os/^{188}Os$ measured in static mode was 0.1198602 ($n = 16$). Brandon et al. (2000) reported an average standard value of 0.1198464 ($n = 28$) for measurements made in dynamic mode on the Sector-54 mass spectrometer at the University of Maryland, College Park. Thus, the static measurements were normalized downward by 0.012%. The bias in analyses in static mode is the result of the slightly differing efficiencies among the Faraday cups. Measurements made in dynamic mode normalize out variations in Faraday cup efficiencies and amplifier gains and provide a more accurate measure of the absolute $^{186}Os/^{188}Os$ ratio (Walker et al., 1997).

3. SAMPLES

3.1. Group IIAB Irons

The group IIAB irons display one of the clearest cases of fractional crystallization of metallic magma during core formation (Scott, 1972). The well-established Ni-Ir trend for the IIAB group defines a very steep negative slope (Fig. 1), indicating a high Ir distribution coefficient and a Ni distribution coefficient near unity. The trend is also consistent with moderately high S content in the parental metallic magma as suggested by Jones and Drake (1983). Some or even most of the scatter of data along the ideal fractional crystallization line is due to the analytical uncertainty associated with the Ni measurement. Scatter in Ni increases when the mean Ni content reaches ~6% because of nonuniform sampling of rare taenite and more common schreibersite. The Ir distribution pattern in IIAB iron meteorites appears to be dominated by fractional crystallization, with only minor complexities for the most evolved irons.

Originally, two separate groups were recognized (IIA and IIB) on the basis of their different crystallographic structure and the prominent hiatus in the Ir content. It is now generally accepted that IIA and IIB iron meteorites originated from the same parent body and were formed sequentially by fractional crystallization of the same magma pool; thus, there is no longer a basis for separation into two subgroups. Samples were chosen to span nearly the complete range of Ni and Ir concentrations reported previously. For convenience in the following discussion, we separate our sample set into high-Os and low-Os irons, with the boundary taken to be 300 ppb Os.

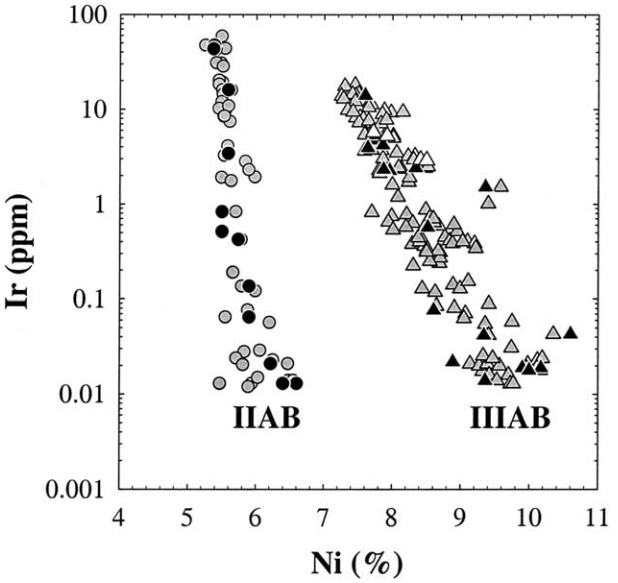

Fig. 1. Plot of Ni (in wt.%) vs. Ir (in ppm) for IIAB and IIIAB irons. Solid symbols are data for meteorites examined by this study. Gray symbols are other IIAB and IIIAB irons. Open triangles are data for the Cape York suite (IIIAB). The limited variation in Ni contents in the IIAB irons is consistent with crystal–liquid fractionation dominated by fractional crystallization. The much larger variation in Ni defined by the IIIAB irons requires mixing processes in addition to fractional crystallization (Wasson, 1999). Data are from Wasson (1999) and Wasson (unpublished data). Note that Ir is plotted on a logarithmic scale.

3.2. Group IIIAB Irons

The IIIAB meteorites are the largest magmatic iron meteorite group, comprising about one-third of all iron meteorites. The recovered mass of the IIIAB group is 4 times greater than that of the next largest magmatic group, the IIAB irons. Thus, the IIIAB group seems to represent a portion of a core of a sizable asteroid. The main-group pallasites (PMG) may also have originated in the same asteroid (Scott, 1977; Clayton and Mayeda, 1996; Wasson and Choi, 2003).

Like the IIAB irons, the IIIAB meteorites were originally classified into separate IIIA and IIIB groups on the basis of trace element chemistry. As with the IIAB group, it is now generally agreed that all IIIA and IIIB irons originated in the same parent core and that there is a continuity of properties (including structure) and thus, no basis for separating into two

Table 1. Rhenium and Os isotopic and composition data for group IIAB and IIIAB iron meteorites. Samples within groups are listed in order of descending Os concentration.

Sample	ID Number	Weight (g)	Ni (%)	Re (ppb)	Blank %	Os (ppb)	$^{187}Os/^{188}Os$	2σ	$^{187}Re/^{188}Os$	2σ	$\Delta \times 10{,}000$	2σ
Group IIAB												
High-Os (IIA)												
Negrillos	USNM1222	0.06	5.25	4893.6	0.01	66847	0.123354	0.000011	0.35252	0.00071	2.3	2.0
Bennett County	USNM 1199	0.08	5.40	4539.0	0.00	58062	0.125143	0.000021	0.37654	0.00075	1.3	2.0
Coahuila	USNM 2725	0.10	5.65	1227.8	0.03	10138	0.141625	0.000023	0.5846	0.0012	2.4	2.0
Filomena	USNM 1334	0.52	5.50	199.61	0.02	1033.4	0.169318	0.000020	0.9357	0.0019	3.1	2.0
Low-Os (IIB)												
Old Woman (o)	USNM 6359B	0.40	5.49	44.69	0.14	253.88	0.162786	0.000020	0.8521	0.0017	3.5	2.0
duplicate		0.21		44.83	0.34	253.65	0.162747	0.000020	0.8556	0.0017	0.4	2.0
Old Woman (h)	USNM 6359A	0.40	5.63	44.61	0.14	252.90	0.162817	0.000033	0.8539	0.0017	2.4	2.0
Navajo	USNM 5601	0.47	5.49	28.21	0.02	174.23	0.157131	0.000019	0.7831	0.0016	1.3	2.0
Mount Joy	USNM 356	0.57	5.78	22.68	0.20	137.67	0.157788	0.000050	0.7969	0.0020	−3.0	2.3
duplicate		0.76		22.88	0.03	137.32	0.158452	0.000019	0.8061	0.0016	−3.6	2.0
Sandia Mountains	USNM 2292	1.48	5.79	8.498	0.13	60.76	0.148253	0.000130	0.6758	0.0014	−3.1	2.0
duplicate		1.13		8.387	0.27	59.30	0.148616	0.000059	0.6834	0.0021	−5.4	3.0
Smithsonian Iron	USNM 1001	2.25	5.55	3.899	0.05	30.09	0.144590	0.000029	0.6258	0.0013	−0.4	2.0
duplicate		2.05		3.876	0.29	30.05	0.144580	0.000058	0.6230	0.0019	1.8	2.0
Central Missouri	USNM 1377	2.19	6.28	1.509	0.14	13.01	0.139179	0.000033	0.5600	0.0011	−2.7	2.0
Santa Luzia	USNM 772	2.23	5.94	0.7135	0.30	7.811	0.130102	0.000078	0.4404	0.0013	0.7	2.0
São Julião d.M.	USNM 267	2.15	5.47	0.7651	0.18	6.192	0.142204	0.000091	0.5966	0.0012	−1.2	2.0
Group IIIAB												
High-Os (IIIA)												
Costilla Peak	USNM 702	0.11	7.46	1429.8	0.02	18675	0.124470	0.000030	0.36874	0.00074	−2.0	2.0
Toubil River	KMAN 627	0.29	7.62	424.88	0.01	3831.7	0.137689	0.000023	0.5350	0.0011	0.5	2.0
Casas Grandes	USNM 369	0.08	7.79	382.45	0.12	3607.7	0.135776	0.000027	0.5113	0.0010	−0.2	2.0
Verkhne-Udinsk	KMAN 62	0.55	7.98	286.65	0.01	2394.4	0.141150	0.000017	0.5778	0.0012	1.7	2.0
Ssyromolotovo	KMAN 65	0.25	7.74	285.53	0.02	2304.8	0.142762	0.000080	0.5980	0.0012	2.1	2.0
Trenton	USNM 2173	0.37	8.48	182.08	0.01	1581.3	0.139139	0.000024	0.5556	0.0011	−1.1	2.0
duplicate		0.79		180.86	0.01	1569.7	0.139150	0.000028	0.5560	0.0011	−1.3	2.0
Delegate	USNM 484	0.36	9.58	147.43	0.01	1515.5	0.132570	0.000023	0.46900	0.00094	0.8	2.0
Charcas	USNM 467A	0.77	7.84	149.40	0.01	1090.9	0.147705	0.000024	0.6616	0.0013	1.9	2.0
duplicate		0.34		148.49	0.01	1083.9	0.147750	0.000012	0.6618	0.0013	2.2	2.0
Susuman	KMAN 2293	0.23	7.74	145.18	0.02	1048.3	0.148020	0.000025	0.6690	0.0013	−0.8	2.0
Tamarugal	USNM 6680	1.42	8.47	36.104	0.03	255.19	0.148936	0.000036	0.6836	0.0014	−2.9	2.0
duplicate		0.49		35.884	0.02	249.99	0.149573	0.000018	0.6936	0.0014	−4.4	2.0
Cape York Suite												
Savik I		0.19	7.72	458.43	0.01	4365.8	0.135373	0.000012	0.50643	0.00076	−0.4	2.0
Woman		0.22	7.92	422.60	0.01	4135.7	0.134356	0.000019	0.49276	0.00074	0.1	2.0
Thule		0.22	8.50	237.73	0.01	2305.8	0.134675	0.000012	0.49722	0.00075	−0.2	2.0
Agpalilik A1–2		0.19	8.33	224.93	0.01	2282.8	0.132878	0.000012	0.47506	0.00071	−0.9	2.0
Agpalilik A1–6		0.55	8.41	229.88	0.01	2268.6	0.134011	0.000011	0.48865	0.00073	−0.1	2.0
Low-Os (IIIB)												
Tieraco Creek	USNM 927	1.66	10.35	3.111	0.13	31.691	0.132867	0.000023	0.4734	0.0009	0.4	2.0
Grant	USNM 836	1.68	9.41	2.834	0.14	23.784	0.140630	0.000034	0.5751	0.0012	−1.4	2.0
Campbellsville	USNM 2572	2.04	8.60	3.511	0.32	17.500	0.17175	0.00015	0.9721	0.0031	0.2	3.4
Thurlow	USNM 545	2.19	10.17	1.405	0.10	14.897	0.130966	0.000052	0.4548	0.0009	−4.2	2.0
Narraburra	USNM 1754	2.14	10.16	1.361	0.10	14.090	0.131754	0.000034	0.4658	0.0009	−4.9	2.0
Chupaderos	USNM 700	2.01	9.96	1.306	0.18	10.643	0.142299	0.000057	0.5924	0.0012	1.8	2.0
Mount Edith	USNM 528	2.20	9.37	0.8012	0.17	4.3743	0.165047	0.000050	0.8872	0.0018	−0.6	2.0
Wonyulgunna	USNM 1747	1.85	9.32	0.9234	0.28	3.8124	0.187687	0.000068	1.1772	0.0035	−0.3	2.8

o = octahedrite; h = hexahedrite; USNM = U.S. National Museum of Natural History; KMAN = Committee on Meteorites, Russian Academy of Sciences.

Ni data are from Wasson (1999 and unpublished). The 2σ uncertainties include uncertainties in blank corrections. "Blank %" is the percentage of the Re blank correction. Δ is the deviation of $^{187}Os/^{188}Os$ of a sample datum from the appropriate IIAB or IIIAB isochron; 2σ uncertainties are in units of per mil.

subgroups. For this study, samples were chosen to span the range of Ni and Ir concentrations reported previously (Fig. 1). Again for convenience in the discussion, we divide the group into high-Os and low-Os, generally consistent with the earlier IIIA and IIIB designations, with the border at 50 ppb Os.

The IIIAB group had a complex crystallization history (Esbensen et al., 1982). For example, the IIIAB field on an Ir-Ni diagram (or Ir-Au) is much wider than can be explained by analytical scatter about the track resulting from ideal fractional crystallization (Fig. 1). Some parallel process (or processes), such as variable degrees of melt trapping/mixing (Chabot and Drake, 1999; Wasson, 1999), generated the apparent scatter.

Esbensen et al. (1982) reported evidence of a complicated crystallization history for the various meteorites associated

Table 2. Platinum and Os isotopic and composition data for group IIAB and IIIAB iron meteorites. Samples within groups are listed in order of descending Os concentration.

Sample	ID Number	Weight (g)	Ni (%)	Pt (ppb)	Os	$^{186}Os/^{188}Os$	2σ	$^{190}Pt/^{188}Os$	2σ	Δ × 100,000	2σ
Group IIAB											
High-Os (IIA)											
Negrillos	USNM 1222	0.06	5.25	38800	66847	0.119823	0.000007	0.0005540	0.0000043	0.6	7.8
Bennett County	USNM 1199	0.08	5.40	39140	58062	0.119840	0.000010	0.0006436	0.0000013	2.3	2.0
Coahuila	USNM 2725	0.10	5.65	32170	10138	0.119842	0.000013	0.0030362	0.0000061	1.0	2.0
Filomena	USNM 1334	0.52	5.50	25340	1033.4	0.119966	0.000012	0.023556	0.000047	0.2	2.0
Low-Os (IIB)											
Old Woman (o)	USNM 6359B	0.40	5.49	18770	253.88	0.120253	0.000012	0.07093	0.00014	−1.5	2.0
duplicate		0.21		18770	253.65	0.120252	0.000009	0.07107	0.00033	−1.7	4.6
Old Woman (h)	USNM 6359A	0.40	5.63	18690	252.90	0.120247	0.000016	0.07092	0.00014	−2.1	2.0
Navajo	USNM 5601	0.47	5.49	16600	174.23	0.120395	0.000010	0.09137	0.00018	−0.4	2.0
Mount Joy	USNM 356	0.57	5.78	14560	137.67	0.120479	0.000010	0.10207	0.00020	1.2	2.0
duplicate		0.76		14410	137.32	0.120470	0.000009	0.10068	0.00020	1.2	2.0
Sandia Mountains	USNM 2292	1.48	5.79	10760	60.76	0.120898	0.000010	0.16984	0.00034	−0.4	2.0
duplicate		1.13		10540	59.30	0.120906	0.000031	0.17025	0.00034	0.2	2.0
Smithsonain Iron	USNM 1001	2.25	5.55	8670	30.09	0.121556	0.000015	0.27595	0.00055	−2.6	2.0
duplicate		2.05		8654	30.05	0.121616	0.000029	0.27577	0.00055	3.5	2.0
Central Missouri	USNM 1377	2.19	6.28	4269	13.01	0.121833	0.000016	0.31414	0.00063	0.6	2.0
Santa Luzia	USNM 772	2.23	5.94	1322	7.811	0.120794	0.000039	0.16175	0.00032	−5.6	2.0
São Julião d.M.	USNM 267	2.15	5.47	1150	6.192	0.120971	0.000052	0.17775	0.00036	1.9	2.0
Group IIIAB											
High-Os (IIIA)											
Costilla Peak	USNM 702	0.11	7.46	17400	18675	0.119839	0.000008	0.0008902	0.0000082	0.9	9.2
Toubil River	KMAN 627	0.29	7.62	14350	3831.7	0.119844	0.000012	0.0035833	0.0000072	−0.3	2.0
Casas Grandes	USNM 369	0.08	7.79	13990	3607.7	0.119859	0.000017	0.0037070	0.0000074	1.1	2.8
Verkhne-Udinsk	KMAN 62	0.55	7.98	13580	2394.4	0.119849	0.000008	0.005428	0.000011	−1.0	2.0
Ssyromolotovo	KMAN 65	0.25	7.74	13250	2304.8	0.119856	0.000007	0.005502	0.000011	−0.3	2.0
Trenton	USNM 2173	0.37	8.48	11430	1581.3	0.119873	0.000012	0.006917	0.000014	0.5	2.0
duplicate		0.79		10820	1569.7	0.119876	0.000016	0.006594	0.000013	1.0	2.0
Delegate	USNM 484	0.36	9.58	8116	1515.5	0.119836	0.000011	0.005119	0.000010	−2.1	2.0
Charcus	USNM 467A	0.77	7.84	12530	1090.9	0.119900	0.000011	0.011000	0.000022	0.5	2.0
duplicate		0.34		11960	1083.9	0.119891	0.000006	0.010573	0.000021	−0.1	2.0
Susuman	KMAN 2293	0.23	7.74	12300	1048.3	0.119882	0.000012	0.011248	0.000022	−1.4	2.0
Tamarugal	USNM 6680	1.42	8.47	7859	255.19	0.119982	0.000016	0.029503	0.000060	−3.1	2.0
duplicate		0.49		7838	249.99	0.120015	0.000010	0.030043	0.000060	−0.1	2.0
Cape York Suite											
Savik I		0.19	7.72	14825	4365.8	0.1198659	0.000006	0.0032466	0.0000065	2.1	2.0
Woman		0.22	7.92	14159	4135.7	0.1198627	0.000009	0.0032729	0.0000065	1.8	2.0
Thule		0.22	8.50	10674	2305.8	0.1198784	0.000006	0.0044257	0.0000089	2.6	2.0
Agpalilik A1–2		0.19	8.33	10511	2282.8	0.1198848	0.000006	0.0044008	0.0000088	3.2	2.0
Agpalilik A1–6		0.55	8.41	12974	2268.6	0.1198824	0.000006	0.005467	0.000011	2.3	2.0
Low-Os (IIIB)											
Tieraco Creek	USNM 927	1.66	10.35	2089	31.691	0.120198	0.000012	0.06303	0.00013	−2.9	2.0
Grant	USNM 836	1.68	9.41	2876	23.784	0.120592	0.000014	0.11945	0.00024	0.4	2.0
Campbellsville	USNM 2572	2.04	8.60	5010	17.500	0.121589	0.000082	0.27504	0.00055	0.6	2.0
Thurlow	USNM 545	2.19	10.17	1388	14.897	0.120387	0.000029	0.08904	0.00018	−0.7	2.0
Narraburra	USNM 1754	2.14	10.16	1511	14.090	0.120464	0.000018	0.10254	0.00021	−1.6	2.0
Chupaderos	USNM 700	2.01	9.96	1505	10.643	0.120649	0.000025	0.13329	0.00027	−2.7	2.0
Mount Edith	USNM 528	2.20	9.37	2448	4.3743	0.123222	0.000027	0.5375	0.0011	−3.9	2.0
Wonyulguma	USNM 1747	1.85	9.32	3338	3.8124	0.125251	0.000035	0.8439	0.0017	3.1	2.0

o = octahedrite; h = hexahedrite; USNM = U.S. National Museum of Natural History; KMAN = Committee on Meteorites, Russian Academy of Sciences.

Ni data are from Wasson (1999 and unpublished). The 2σ uncertainties include uncertainties in blank corrections. Δ is the deviation of $^{186}Os/^{188}Os$ of a sample datum from the appropriate IIAB or IIIAB isochron; 2σ uncertainties are in units of per mil.

with the Cape York shower. This suite consists of several large individuals having a total mass of 57 tons, making it the world's second largest recovered iron meteorite. Esbensen et al. (1982) reported correlated compositional variations between the individuals of the Cape York suite that are far larger than have been found in any individual IIIAB iron. For example, concentrations of Ir (and Au) range over factors of ~1.8 (Fig. 1), whereas the range of these elemental concentrations reported within other individual irons had never exceeded experimental uncertainties of ≈ ±4%. Measurable concentration ranges are even observed within one mass of Cape York (Agpalilik). Thus, to further clarify the processes that created these large variations, and possibly obtain an internal isochron age, we analyzed five samples from the Cape York suite.

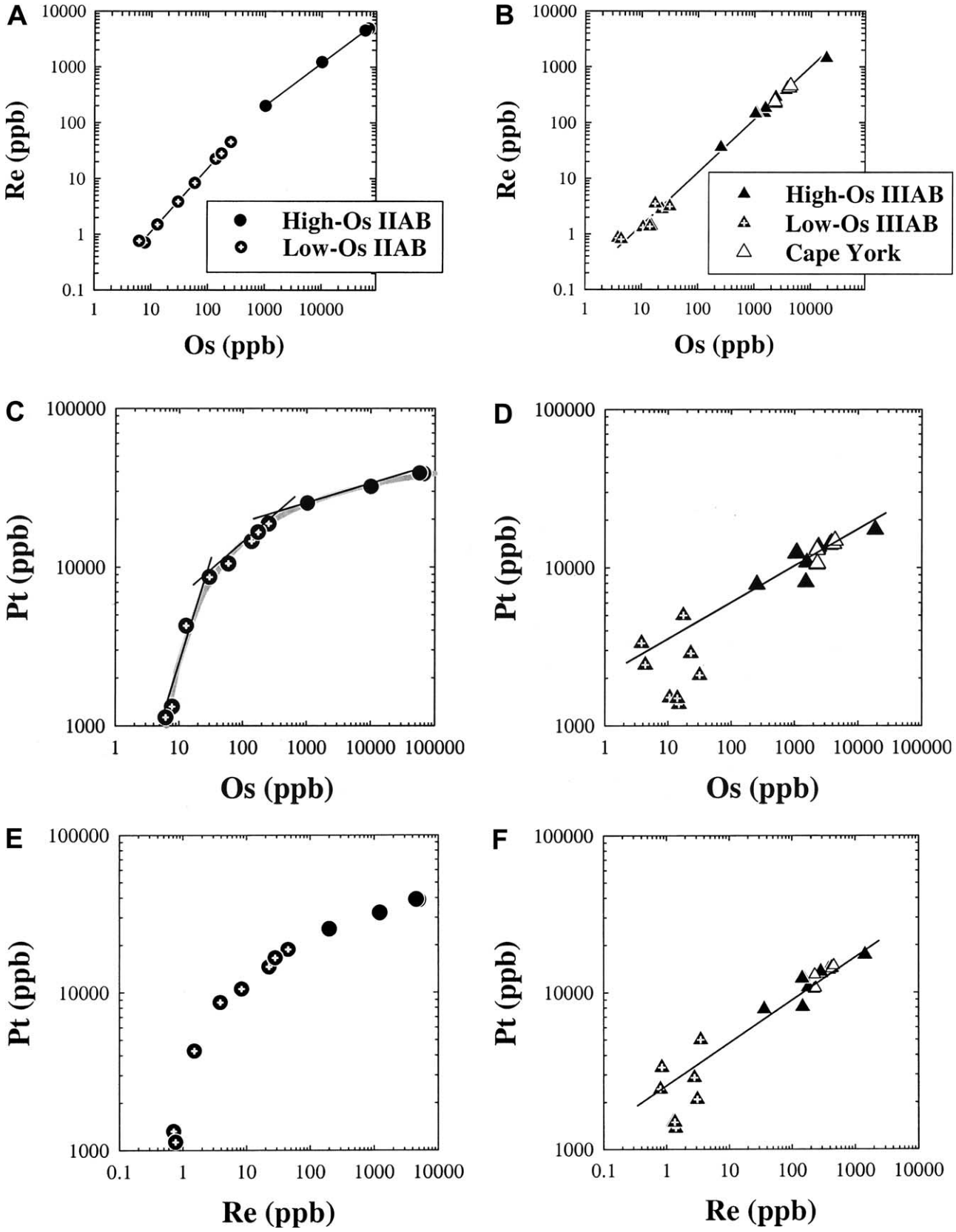
A
Re (ppb)
Os (ppb)
High-Os IIAB
Low-Os IIAB
B
Re (ppb)
Os (ppb)
High-Os IIIAB
Low-Os IIIAB
Cape York
C
Pt (ppb)
Os (ppb)
D
Pt (ppb)
Os (ppb)
E
Pt (ppb)
Re (ppb)
F
Pt (ppb)
Re (ppb)

4. RESULTS

Isotopic and concentration data for the IIAB and IIIAB iron meteorites are summarized in Tables 1 and 2. The reported $^{187}Re/^{188}Os$ and $^{190}Pt/^{188}Os$ ratio 2σ uncertainties include the combined uncertainty in the isotopic measurements and blank corrections. Not included is the uncertainty in the calibration of the Os spike, which is due to uncertainties in the stoichiometry of the Os standard used for spike calibration (Morgan et al., 1995; Yin et al., 2001). The Os and Re blank corrections introduced maximum uncertainties of ±0.1% for most samples. Similarly, the maximum uncertainties in $^{187}Re/^{188}Os$ and $^{190}Pt/^{188}Os$ were ±0.2% for all samples except the IIAB Negrillos, and the IIIAB Costilla Peak, with uncertainties in $^{190}Pt/^{188}Os$ of 0.78% and 0.92%, respectively. These large uncertainties are the result of an unusually large apparent chemical blank associated with one set of chemistry during which these two samples were processed.

Rhenium concentrations range from 0.71 to 4900 ppb and from 0.80 to 1400 ppb in IIAB and IIIAB irons, respectively. Osmium concentrations range from 6.2 to 67,000 ppb and from 3.8 to 19,000 ppb in IIAB and IIIAB irons, respectively. In contrast to the large range in concentrations for Re and Os, Pt concentrations range only from 1100 to 39,000 ppb and from 1400 to 17,000 ppb in IIAB and IIIAB irons, respectively. The concentration ranges are consistent with those reported by previous studies (Pernicka and Wasson, 1987; Morgan et al., 1995; Chen et al., 2002), although the Pt concentrations presented here average ~8% higher than those reported by Pernicka and Wasson (1987). On a logarithmic plot, variations in the concentrations of Re and Os for the IIAB irons are generally linear, but with a change in slope at ~300 ppb Os (Fig. 2a). The concentrations of Re and Os for the IIIAB irons also co-vary in a generally linear manner but are more scattered (Fig. 2b). No change in slope along the trend is discernible. The Cape York suite plots along the main trend of data (Fig. 2b).

On a logarithmic plot of Pt vs. Os for IIAB irons (Fig. 2c), concentrations co-vary with Pt becoming increasingly depleted relative to Os as the overall concentrations of these elements decrease. The IIIAB irons define a much more scattered trend that is similar in slope to the trend defined by high-Os IIAB irons but with lower relative concentrations of Pt (Fig. 2d). The Cape York suite plots within the Pt-Os envelope defined by the other high-Os irons. There is particularly large scatter among the most evolved, low-Os IIIAB irons.

The logarithmic plot of Pt vs. Re for IIAB irons defines a relatively smooth curve (Fig. 2e). The logarithmic plot of Pt vs. Re for IIIAB irons is very similar to that of the Re vs. Os plot (Fig. 2f), with substantial scatter in the most evolved, low-Os IIIAB irons.

Elemental ratios also vary in a systematic way. For IIAB irons, the $^{187}Re/^{188}Os$ ratios increase from 0.35 to 0.94 during crystallization of high-Os irons, then begin to decrease during crystallization of low-Os irons, eventually returning to the chondritic value of approximately 0.4 (Fig. 3a), as has been noted by previous studies (Morgan et al., 1995; Shirey and Walker, 1998; Chen et al., 2002). Only the low-Os iron, São Julião de Moreira plots somewhat off this trend. In contrast, the IIIAB irons are highly scattered. The $^{187}Re/^{188}Os$ ratios increase from 0.37 to 0.68 for high-Os irons, then begin to decrease slightly for most of the low-Os irons (Fig. 3b). Three of the low-Os irons, Campbellsville, Wonyulgunna, and Mount Edith, deviate from this trend with $^{187}Re/^{188}Os$ ratios that are significantly higher than chondritic (0.89 to 1.2). The four samples from the Cape York suite display a nearly twofold variation in Re and Os concentrations but only a modest 6% variation in $^{187}Re/^{188}Os$.

With decreasing Pt, the $^{190}Pt/^{188}Os$ ratios for IIAB irons increase from 0.00055 to a maximum ratio of 0.31 (Fig. 3c). A slight decrease in the $^{190}Pt/^{186}Os$ ratio occurs at the lowest Pt portion of the trend, although all the ratios for low-Os samples remain well above the chondritic ratio of approximately 0.0017. The $^{190}Pt/^{188}Os$ ratios of most IIIAB irons plot on a roughly linear trend that increases from 0.00089 to 0.53 with decreasing Pt (Fig. 3d). This trend is offset to lower Pt concentrations, but the slope is similar to the mean slope for the IIAB irons. Platinum concentrations within the Cape York suite vary only by approximately 40%, whereas $^{190}Pt/^{188}Os$ ratios vary by nearly 70%

5. DISCUSSION

5.1. Fractionation Trends in Group IIAB and IIIAB Irons

Variations in the abundances of Re, Os, Pt, and other highly siderophile elements (HSE), for both the IIAB and IIIAB systems, were dominated by solid metal–liquid metal partitioning as crystal–liquid fractionation proceeded. Nonmetal phases, such as sulfides and phosphides, that crystallized from pockets of trapped melt, contain much lower abundances of Re and Os than metal phases, so their crystallization likely had only very minor impacts on the fractionation and possibly the fractionation of Re, Os, and the other HSE in these metal-dominated systems (Shen et al., 1996). The magnitude of solid metal–

Fig. 2. (a–b) Osmium (in ppb) vs. Re (in ppb) plot for (a) IIAB iron meteorites and (b) IIIAB irons. High-Os and low-Os IIAB irons define linear trends with slopes of 0.773 ± 0.027 and 1.142 ± 0.035 (regression errors are 2σ), respectively. Note that both axes are logarithmic. High-Os and low-Os IIIAB irons define linear trends with slopes of 0.865 ± 0.048 and 0.76 ± 0.38, respectively. Collective regression of all IIIAB data yields a slope of 0.950 ± 0.035 (shown). (c–d) Osmium (in ppb) vs. Pt (in ppb) plot for (c) IIAB iron meteorites and (d) IIIAB irons. Note that both axes are logarithmic. The plot for IIAB irons is nonlinear but can be fitted to a second-order polynomial function $\log[Pt] = 4.878 - 1.444/(\log[Os]) - 0.0236/(\log[Os])^2$ (gray curve). Correlated changes in Pt relative to Os can be obtained from the slopes of tangents fitted to the curve along the fractionation trend. Starting with the high-Os irons, tangents with slopes of 0.105, 0.327, and 1.05 are shown. The data for IIIAB irons are highly scattered and can not be fitted with either a line or a curve. (e–f) Rhenium (in ppb) vs. Pt (in ppb) plot for (e) IIAB iron meteorites and (f) IIIAB irons. Note that both axes are logarithmic. As a consequence of the high linearity between Os vs. Re, the plot for IIAB irons yields a curved array similar to that generated for Os vs. Pt. The data for IIIAB irons are highly scattered.

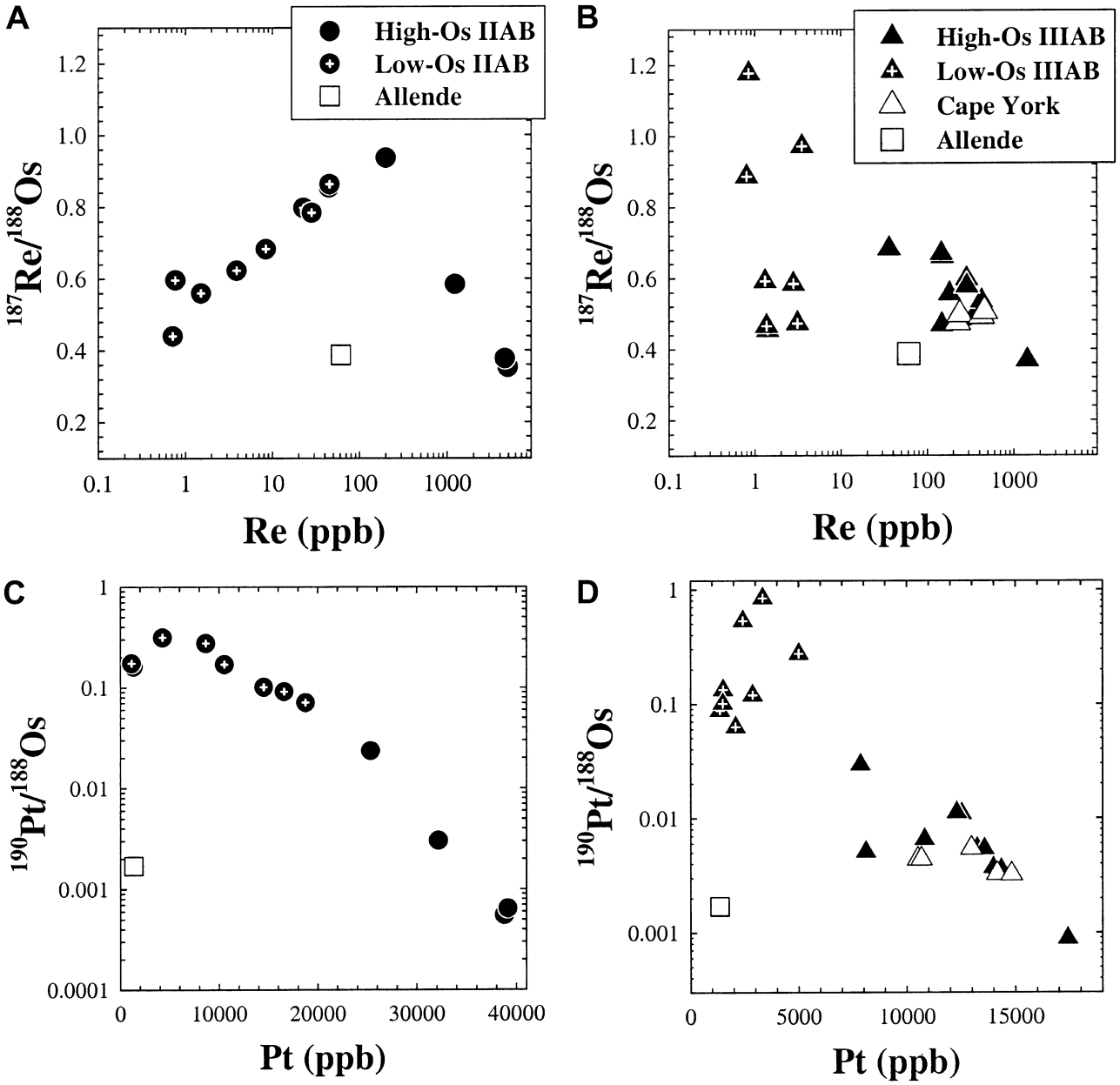

Fig. 3. (a–b) Rhenium (in ppb) vs. $^{187}Re/^{188}Os$ for (a) IIAB and (b) IIIAB irons. Data for Allende are from Walker et al. (2002). Note that the Re scale is logarithmic. The $^{187}Re/^{188}Os$ ratios increase with decreasing Re for high-Os IIAB irons and decrease with decreasing Re for low-Os IIAB irons. A major break in slope occurs near Re = 100 ppb. Similarly, the $^{187}Re/^{188}Os$ ratios of high-Os IIIAB irons increase with decreasing Re. Unlike for IIAB irons, this general trend continues to three highly evolved, low-Os irons (Campbellsville, Mount Edith, and Wonyulgunna), with $^{187}Re/^{188}Os$ ratios ≥ 0.887. The remaining low-Os IIIAB irons have much lower $^{187}Re/^{188}Os$ ratios similar to the most evolved (lowest Re and Os) IIAB irons. (c–d) Platinum (in ppb) vs. $^{190}Pt/^{188}Os$ for (a) IIAB and (b) IIIAB irons. Data for Allende are from Walker et al. (2002) and Horan et al. (2003). The IIAB irons define a general trend to higher $^{190}Pt/^{188}Os$ with decreasing Pt. The most highly evolved irons (lowest Os and Pt) display a modest decrease in $^{190}Pt/^{188}Os$. The data for IIIAB irons are moderately scattered but define a general trend toward increasing $^{190}Pt/^{188}Os$ with decreasing Pt.

liquid metal partitioning of the HSE has been intensively explored via both experimental studies and the examination of natural systems (e.g., Jones and Malvin, 1990; Morgan et al., 1995; Walker, 2000). In brief, experimental studies have shown that D values for HSE between solid metal and liquid metal are primarily controlled by the abundances of certain constituents present in the liquid, particularly S and P. In general, Re and Os become increasingly compatible with solid metal as S and/or P contents in the liquid increase during the normal crystallization sequence of metal systems (Narayan and Goldstein, 1982; Jones and Drake, 1983; Jones and Malvin, 1990; Walker, 2000). Platinum shows more complex behavior; D values can both increase and decrease with increasing S and P (Walker, 2000). Despite their major control on D values, the contents of

S and P in the parental liquids of magmatic iron systems are very difficult to estimate. This is because of the extreme incompatibility of S and incompatibility of P in the precipitating metal that we ultimately sample.

There has been debate regarding whether or not D values for some or all of the HSE changed during crystallization of magmatic iron groups, especially the IIAB system (Jones, 1994; Morgan et al., 1992; Morgan, 1995; Jones, 1995). This conundrum has arisen because experiments on synthetic systems provide unambiguous evidence for changing D values as S and P contents vary with extent of crystal–liquid fractionation (Jones and Drake, 1983; Jones and Malvin, 1990; Chabot et al., 2003). Conversely, linear trends on log-log diagrams were interpreted to be more consistent with constant D values over much of a crystallization sequence (Morgan et al., 1995). For plots of log[X] vs. log[Y]:

$$Slope\ of\ correlation = (D_Y - 1)/(D_X - 1) \quad (1)$$

A linear array requires that either D values are constant for both elements, or that changes in the D value for one element are offset by changes in the other in such a manner as to retain a near constant ratio of $(D_Y - 1)/(D_X - 1)$. Morgan et al. (1995) concluded that the high degree of linearity of the log[Os] vs. log[Re] plot for high-Os and low-Os IIAB irons is not consistent with significant changes in D values for these two elements.

Although the absolute D values and constancy of D values for crystallizing iron systems remain difficult to constrain, the *relative* solid metal–liquid metal partitioning characteristics of certain HSE over some portions of a crystallization sequence can be estimated from the natural systems, assuming a closed system. This is important as it allows the prediction of composition trends and ratio changes for these elements. As noted, relative D_{Re} and D_{Os} values have been previously examined and discussed in detail with regard to the IIAB system (e.g., Morgan et al., 1995). The present work permits the addition of Pt to the comparison. Estimations of relative D values for solid metal–liquid metal partitioning can be made using the slopes obtained from trends on log-log plots of abundance (Fig. 2a–f). On such plots, the slopes of the trends can be used to estimate D_{Re} and D_{Pt} relative to D_{Os} from Eqn. 1. For elemental plots that show curved trends, relative D values can be estimated from the slopes of tangents to the best-fit curves.

5.1.1. IIAB Irons

Most D values for HSE in iron meteorite systems have been calculated previously relative to D_{Ir}, the D value for which there are the most concentration and experimental partitioning data for metal systems. We will continue that practice here. For early stages of crystallization of the high-Os IIAB hexahedrites, Morgan et al. (1995) used an experimentally determined D_{Ir} of 14.0 for a system with initially 17 wt.% S (Jones and Drake, 1983) and estimated a corresponding D_{Os} of 18.9 from the linear correlation between log[Os] and log[Ir]. For consistency with previous studies, the D_{Os} of 18.9 will also be used here as the point of comparison in subsequent calculations of relative D values for Pt and Re.

From the linear regression of the data and the assumption of this D_{Os}, the relative D values for Re and Pt of the group IIAB irons are obtained. Linear regressions of data for log[Os] vs. log[Re] are shown in Figure 2a. Slopes for the log[Os] vs. log[Re] trends (high-Os = 0.773 ± 0.027; low-Os = 1.142 ± 0.035; errors are 2σ) yield calculated D_{Re} for the high-Os and low-Os IIAB irons of 14.8 and 21.4, respectively, for a constant D_{Os} of 18.9. It is emphasized that these D values serve only as relative points of reference. If D_{Os} increased with increasing degree of fractionation, as seems likely, D_{Re} (and D_{Ir}) would also have increased correspondingly to maintain a constant ratio for $(D_{Re} - 1)/(D_{Os} - 1)$. Note that for the assumption of closed-system core crystallization, the decrease in $^{187}Re/^{188}Os$ in the low-Os IIAB as crystal–liquid fractionation proceeded requires a major increase in the compatibility of Re relative to Os (Fig. 3a).

The log[Os] vs. log[Pt] trend for IIAB irons (Fig. 2c) is nonlinear and more complicated than the Os vs. Re trend. The data can be fitted to a second-order polynomial function where: $\log[Pt] = 4.878 - 1.444/(\log[Os]) - 0.0236/(\log[Os])^2$. Correlated changes in Pt relative to Os can be obtained from the slopes of tangents fitted to the curve along the fractionation trend. Tangents with slopes of 0.105, 0.327, and 1.05 are shown in Figure 2c for high-, moderate-, and low-Os IIAB irons. Tangents during early and late stages of IIAB evolution indicate an initial D_{Pt} of approximately 3, and a value of approximately 20 during the end stages of crystallization. Again, these values are calculated relative to a constant D_{Os} value of 18.9. This suggests that for the IIAB system, Pt was only mildly compatible during the early stages of crystallization, but became even more highly compatible than Os during the late stages of crystallization, as is also indicated by decreasing $^{190}Pt/^{188}Os$ ratios for the most evolved samples (Fig. 3c). If the D_{Os} increased during the crystallization sequence to a value substantially greater than 18.9, as suggested by experimental studies, then D_{Pt} would have consequently been significantly >20.

5.1.2. IIIAB Irons

There is a generally linear trend defined for log[Os] vs. log[Re] for the high-Os IIIAB irons, with a slope of 0.865 ± 0.048 (Fig. 2b). The correlation for the low-Os irons is much more poorly defined, with a slope of 0.76 ± 0.38. Collectively, a regression of the plot of log[Os] vs. log[Re] for the entire IIIAB system produces a relatively linear array with a slope of 0.950 ± 0.035 (Fig. 2b). As with the IIAB system, Os is more compatible than Re during initial stages of crystallization of the IIIAB core, accounting for the increase in Re/Os ratio as the high-Os irons crystallized. Unlike for the IIAB system, three of the eight low-Os irons analyzed have higher Re/Os than the most evolved high-Os irons (Fig. 3b). This could indicate that only a portion of the IIIAB system evolved to conditions under which Re became more compatible than Os, or that the low-Os irons were generated via another type of process, such as solid-melt mixing. Concentration of some HSE in minor phases and distribution between taenite and kamacite may also have played roles.

To make estimates of relative D values for Os and Re during IIIAB crystallization, D_{Ir} is again used as the point of comparison. The D_{Ir} for the initiation of crystallization of the high-Os IIIAB irons was discussed by Wasson (1999) who concluded

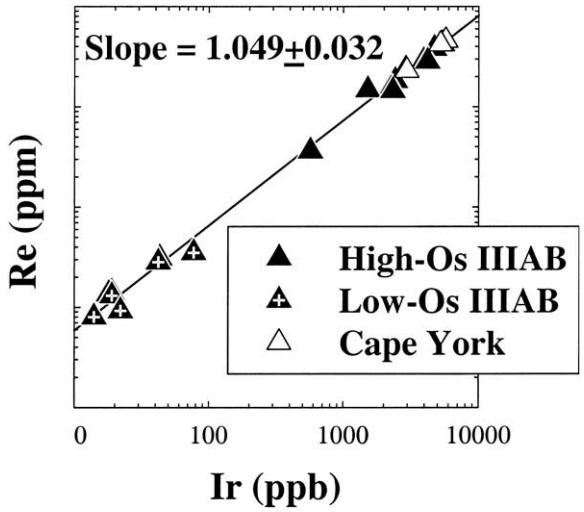

Fig. 4. Iridium (in ppb) vs. Re (in ppb) for IIIAB irons. Note that both axes are logarithmic. Data define a well-defined linear trend with a slope of 1.049 ± 0.032 (2σ). Iridium data are from Wasson (1999) and Wasson (unpublished data).

that a D_{Ir} of 4.5 was appropriate for modeling initial stages of IIIAB crystallization, assuming starting S and P contents of 20 and 4.8 mg/g, respectively. The regression of log[Ir] vs. log[Re] for high-Os IIIAB irons, generated using the new Re data combined with Ir data (Wasson, 1999, and unpublished data), gives a slope of 1.049 ± 0.032 (this is used because it is a better correlation than for Ir-Os) (Fig. 4). From this correlation, an initial D value for Re of 5.0 is calculated. A D_{Os} value of 5.5 is calculated relative to D_{Re} using the slope of 0.865 for log[Os] vs. log[Re], for the high-Os irons. Wasson (1999) concluded that the D value for Ir during the latter stages of IIIAB crystallization rose to 7.7 as the S content of the liquid changed from ~20 mg/g (100% liquid) to 100 mg/g (20% liquid). Given the general linearity of log[Os] vs. log[Re] and log[Ir] trends throughout the IIIAB crystallization sequence, this would require that D_{Re} and D_{Os} also increased in a corresponding manner, such that D values may have risen to ca. 8.3 and 9.2, respectively, at 80% crystallization.

Plots of log[Re] and log[Os] vs. log[Pt] for IIIAB irons are highly scattered and do not yield linear trends or highly correlated curved trends (Fig. 2d,f). The data for the most evolved, low-Os IIIAB irons are particularly scattered. This suggests that D_{Pt} was potentially quite variable relative to either Re or Os. It is also possible that sampling biases could have affected Pt abundances more significantly than Re or Os. While data exist to indicate that schreibersite, for example, excludes Re and Os from its structure (Shen et al., 1996; Birck and Allègre, 1998), no similar data exist for Pt. It is, therefore, possible that biased sampling of nonmetal phases having high Pt abundances may be responsible for some or all of the variations. Nonetheless, Pt must have been much less compatible than Os for most or all of the IIIAB crystallization sequence resulting in the general evolution to high $^{190}Pt/^{188}Os$, as Os (and Pt) abundances decreased (Fig. 3d). Given the scatter of the data, however, no stricter constraints on the relative D_{Pt} can be generated from these relations.

5.2. Mixing of Liquid and Solid: Three Processes

Several processes have been invoked to account for the distributions of various elements within the IIIAB iron system. For example, Esbensen et al. (1982) noted that the large difference between the extreme compositions of the members of the Cape York suite could be understood if they were formed as variable mixtures of equilibrium solid and melt. Consistent with this view, Agpalilik, at the lower-Os, higher-Ni end of the suite, was observed to have ~9–10 times more S than Savik, the member at the higher-Os, lower-Ni end of the array (Wasson, 1999). From this trend, Esbensen et al. (1982) estimated the initial S content of the IIIAB magma to be ~14 mg/g.

Haack and Scott (1993) noted that in IIIAB irons, fractional crystallization alone cannot explain the relatively large variations in the concentrations of some elements away from an ideal fractional crystallization trend (e.g., Fig. 1). They concluded that some IIIAB irons, such as some of the Cape York suite, Treysa and Delegate, were generated via the mixing between early-formed solids and evolved liquids.

Wasson (1999) reexamined the formation of group IIIAB irons (and the Cape York suite) using an augmented data set and modally estimated S contents of IIIAB irons. That study employed numerical simulations of the crystallization of the IIIAB magma, and modeled revised data for the Cape York irons Savik I and Agpalilik to estimate the initial S content of the IIIAB magma and obtained 20 mg/g. Wasson (1999) concluded that the compositions of most IIIAB irons reflect the presence of variable proportions of trapped melt, and that in most IIIAB irons, except three or four (Treysa, Delegate, Tieraco Creek, and possibly Ilinskaya Stanitsa), the trapped melt could be equilibrium melt.

Chabot and Drake (1999) considered the possibility of mixing between a relatively evolved liquid and a second, more primitive liquid during the course of core crystallization. In their model, the evolved liquid is active in the crystallization process, whereas the more primitive liquid is envisioned as too distant from the crystallization front to be actively involved in the crystallization process.

Our new, high-precision Re and Os concentrations allow us to model these elements and compare the results with the models generated for other trace element pairs. Given the complexities in the interpretation of D_{Pt} in the IIIAB system, no attempt will be made to model Pt. It is important to note that the general adherence of the samples to primordial Re-Os (and Pt-Os) isochrons (see below) is strong evidence that the ratios of these elements have not been modified by more than about ±1% subsequent to formation of the octahedral structures. Here, we consider the behavior of Re and Os via mixing of liquids and solids as a function of three interrelated liquid–solid mixing processes. In an actual core, an infinite number of different mixing processes are possible, but it is useful to discuss the fractionations introduced by the following three processes: 1) equilibrium melt was trapped within coexisting solids; 2) evolved melt was mixed with earlier crystallized solids; and 3) primitive mantle-derived melt was added to evolved melt. The latter process is mathematically similar to the two liquid model of Chabot and Drake (1999). We illustrate these processes in Figure 5a–c.

The first process (Fig. 5a) involves mechanical trapping of

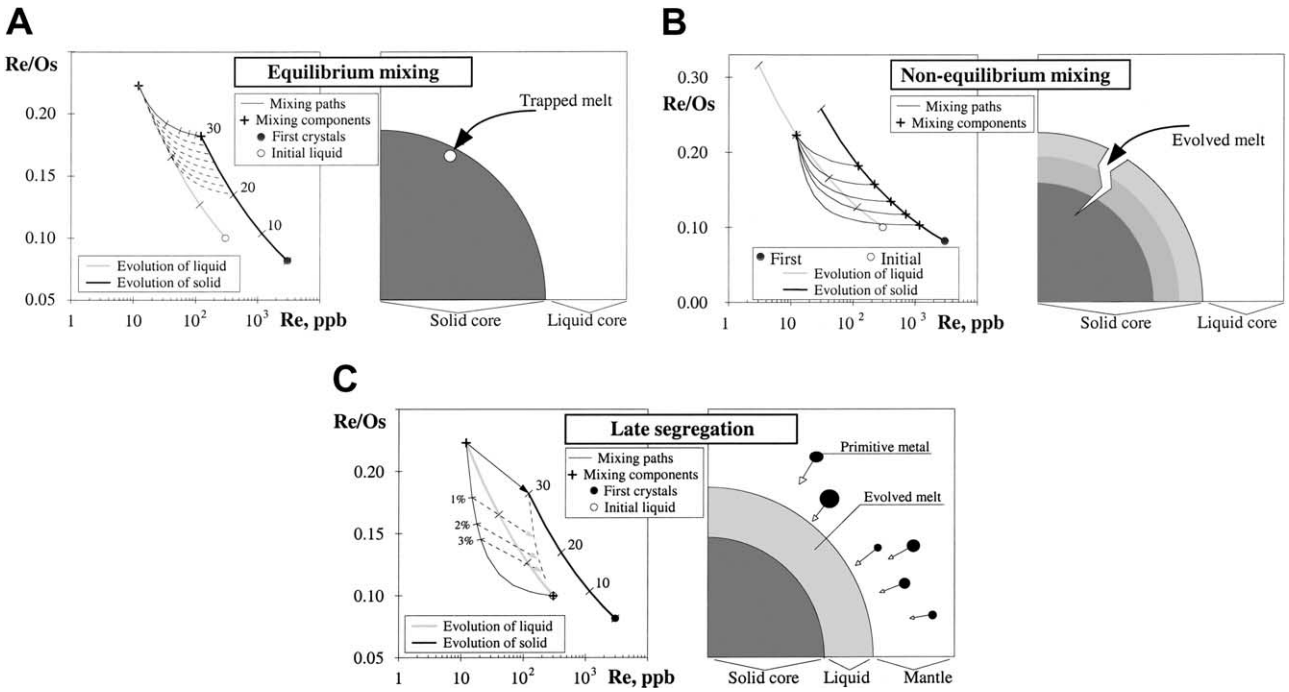

Fig. 5. (a) Re-Os distribution patterns produced by mixing of an evolved melt with the corresponding equilibrium solid (equilibrium mixing). The right drawing shows schematically a portion of the melt that was sealed in a cavity. The surrounding solid is of the equilibrium composition with respect to the trapped liquid. After solidification, mixing with the wall material results in a composition that falls along a line which is shown on the left plot as a thin solid line. Tick marks on this line denote a percentage of trapped liquid in the mixtures, in 20% increments. In this example, mixing was assumed to happen at 30% of the main crystallization sequence (the tick marks on the evolution trends denote the percentage of the main crystallization in 10% increments). This kind of mixing, if it occurs continuously, could produce samples that fill in the space between the two main evolution trends, as shown in the left plot by the dashed lines. From Smoliar (1996). (b) Re-Os distribution pattern produced by mixing of an evolved melt with early fractions of solid (nonequilibrium mixing). Right cartoon illustrates that this kind of mixing can occur along a tectonic fracture in the crystallizing core. The different shading of the solid core illustrates schematically different compositions so that the compositional contrast between melt and walls increases with depth. The left plot shows the corresponding mixing lines (thin solid lines) with respect to main crystallization trends (thick solid and gray lines). The uppermost mixing line is essentially the previous case of mixing of the melt trapped in the equilibrium solid (because the upper part of fracture walls is composed of crystals equilibrated with the melt). An important feature of this type of mixing is that it can produce materials plotting to the left of the liquid crystallization trend (shaded area). From Smoliar (1996). (c) Re-Os distribution pattern produced by mixing of an evolved melt with a liquid metal of primitive composition. The right cartoon shows this kind of mixing as a result of late segregation, assuming a few percent of metal were left in the mantle during the main core segregation; this metal gradually joins the core substantially later, when the core is partially crystallized. The left diagram shows the Re-Os distribution in this process. For this example, the 30% stage of fractional crystallization was chosen, i.e., 30% of the total mass of the core is solid. With respect to Re and Os, the residual liquid is already quite different from the initial composition: its Re/Os ratio is more than a factor of two higher, and it is depleted in Re and Os by about a factor of 20. Because of such depletion, the evolved melt is quite sensitive to addition of primitive liquid metal; even 1% of primitive metal makes a significant change in the Re/Os ratio of the resulting liquid. The change in the liquid composition causes a corresponding change in the composition of the solid forming (dashed arrows). All solids forming via crystallization of the mixed liquids would plot in the region between the evolution tracks for liquids and solid (as with equilibrium mixing). From Smoliar (1996).

melt between dendrites or other surface irregularities (Narayan and Goldstein, 1982; Haack and Scott, 1992), or by the detachment and fall of roof pendants (Esbensen et al., 1982). On a plot of Re/Os ratio vs. Re, solid–liquid mixtures plot on curves that connect the compositions of the corresponding equilibrium solids and liquids.

The second process (Fig. 5b) involves the mixing of evolved (depleted in Re and Os) melt with an early-crystallized solid that is enriched in refractory HSE. This type of mixing can be envisioned as an injection of liquid into fractures in the solid core; in most cases the liquid fraction dominates, suggesting the incorporation of wall rock. Detachment of a large block from the ceiling of the magma chamber might produce the same kind of mixture in the void vacated by the block. Compositions plot along liquid–solid mixing curves and, because the components can be quite different in composition, the resulting mixtures can have wide ranges in absolute concentrations and in Re/Os ratios. It is important to note that, in contrast to "equilibrium mixing," this type of mixing can produce compositions plotting to the left of the liquid track of the fractional crystallization trend.

The third process (Fig. 5c) involves the mixing of evolved melt with late mantle melt. This melt may have a composition similar to that of the chondritic building blocks of the asteroid, but if it represents a second extraction, it should be more refractory than the melt that left the mantle to form the core. Thus, this later metal would have had relatively high Os and Re

concentrations, and a Re/Os ratio that was generally similar to or lower than that of the chondritic precursor. Because the evolved core liquid would be depleted in Re and Os, a minor addition of primitive or refractory melt added to the residual melt would cause a significant decrease in the Re/Os ratio of an evolved magma. Solids resulting from the crystallization of mixing between primitive and evolved melts would generally plot between the original liquid and solid tracks calculated for simple fractional crystallization. If, however, trapped melt fractions were large, the solid compositions could plot to the left of the original liquid track. Additions of more than a few percent of primitive melt to the system drives the Re/Os ratio of precipitating solids back toward a chondritic ratio and relatively high concentrations of HSE. This process has been previously suggested to produce the essentially chondritic Re/Os ratios in highly evolved, low-Os IIAB irons (Pernicka and Wasson, 1987).

In real asteroids the first two processes appear to have occurred, and the third process may also have contributed (Pernicka and Wasson, 1987; Wasson, 1999). We now consider how these processes might explain our Re-Os observations. Two fractional crystallization models consistent with mixing process 2 can account for the Re-Os abundances and Re/Os ratios of IIIAB irons, but encounter other plausibility problems. The pure endmember mixing process 1 is physically plausible but, as noted in earlier studies, some irons must still be explained by process 2. A model based on process 1 can only account for the bulk of the Re-Os data if there are large sampling errors. Pure process 3 makes predictions that are similar to process 2.

The models presented serve to illustrate the effects of using different starting compositions and D values on predicted crystal–liquid fractionation paths. In model 1 we examine the possibility that most IIIAB formed as equilibrium mixtures of solid and liquids. Solid and liquid tracks for a system with D_{Re} and D_{Os} values varying from 5.0 to 8.3 and 5.5 to 9.2, respectively, are shown in Figure 6a. The variations in D values are consistent with 0-80% fractional crystallization of a system with S ranging from 20 to 99 mg/g and P ranging from 4.8 to 20 mg/g, utilizing the parameterization approach of Jones and Malvin (1990), but D values fitted to the data following Wasson (1999) and consistent with the slope of 0.865 on the plot of log[Os] vs. log[Re] for the high-Os IIIAB irons. For this model, the bulk core is defined as: Re = 470 ppb; Os = 5650 ppb; and a chondritic $^{187}Re/^{188}Os = 0.40$ (approximately the bulk solar system ratio; Becker et al., 2001). These concentrations were chosen so that the initial crystallizing solids would have concentrations that approximate the highest concentrations found in IIIAB irons (e.g., Picacho 2190 ppb; Wasson, unpublished data).

Although this model accounts for the general increase in the Re/Os trend in IIIAB, a major problem with the model is that most of the data plot outside the region bounded by the solid and liquid tracks, i.e., the region where most samples plot on Ir-Au diagrams (Wasson, 1999). Of the high-Os IIIAB irons, only Tamarugal and the Cape York Thule and Agpalilik specimens plot within this region. Costilla Peak plots near a mixing curve connecting the initial solid and liquid. None of the low-Os IIIAB irons plot between the liquid and solid tracks. Hence, neither equilibrium mixing (process 1) nor late-stage metal additions (process 3) can solely explain the majority of the low-Os irons for this starting composition and set of D values. Taken at face value, the data indicate that equilibrium mixing, as proposed by Wasson (1999), cannot account for most IIIAB data. To make some data consistent with an equilibrium mixing model would require either a higher Re/Os ratio in the initial melt or large sampling errors, or a combination of both. Formation of a core with a suprachondritic Re/Os ratio is possible since some residual refractory Fe-Ni metal having low Re/Os ratios will have been left behind in the mantle during core formation, and more refractory metal may have been trapped in silicates. There is no simple way to assess sampling errors; undoubtedly kamacite/taenite ratios vary by small amounts from sample to sample, but the Re/Os ratios in these phases are poorly known, and other minor phases such as phosphides and nitrides may have high concentrations of one or the other element. Simulations show that a starting $^{187}Re/^{188}Os$ ratio around 0.48 or 1σ relative errors $\geq$6% would be required to explain most of the high-Os IIIAB samples by equilibrium mixing. A careful assessment of partitioning of Re and Os between major and minor phases will ultimately be necessary to show whether such large sampling errors are possible.

Low-Os samples plotting well to the left of the liquid track can not be accounted for as equilibrium mixes, even with these assumptions. Instead, they can be explained as mixtures of evolved liquid with solids that crystallized early. For example, Thurlow and Narraburra can be modeled as a mixture of the liquid remaining after 80% crystallization and solid formed after 20% crystallization; for this model, approximately 99.9% of the meteorite would consist of the evolved liquid component.

In model 2 (Fig. 6b) we again attempt to model most IIIAB irons as having formed as equilibrium mixtures. In contrast to model 1, we have chosen D values that give a larger spread between the solid and liquid tracks; the initial Re and Os concentrations are the same as model 1, but D values are much higher, with D_{Re} and D_{Os} varying from 13.0 to 14.5 and 14.9 to 16.6, respectively, over the course of the 0 to 50% fractional crystallization modeled. These D values are plausible if the total S and P contents of the bulk core were higher than estimated by Wasson (1999). The higher D values used in this model are more consistent with the starting S content of 12.5 wt.% used by Chabot and Drake (1999) in modeling other trace elements in the IIIAB system. A major effect of the higher D values is the increased spread between liquid and solid tracks. In comparison to model 1, all high-Os IIIAB irons, including all the Cape York suite and Costilla Peak, plot near or within the two tracks. Thus, all high-Os and two of the low-Os iron compositions can be generated via equilibrium mixing of liquids and solids. For this model, mixing between an evolved liquid generated by 45% fractional crystallization, and solids formed after 10% fractional crystallization can give concentrations consistent with the low-Os Narraburra and Thurlow. A weakness with this model is the prediction of the formation of solids with concentrations that are significantly higher than are observed for group IIIAB irons. In addition, trends in other trace elements, such as Au, Ga, and Co, may not be consistent with such high S contents (Wasson, 1999). Finally, for this model, almost all IIIAB compositions are achieved before 50% fractional crystallization; thus, it requires that later frac-

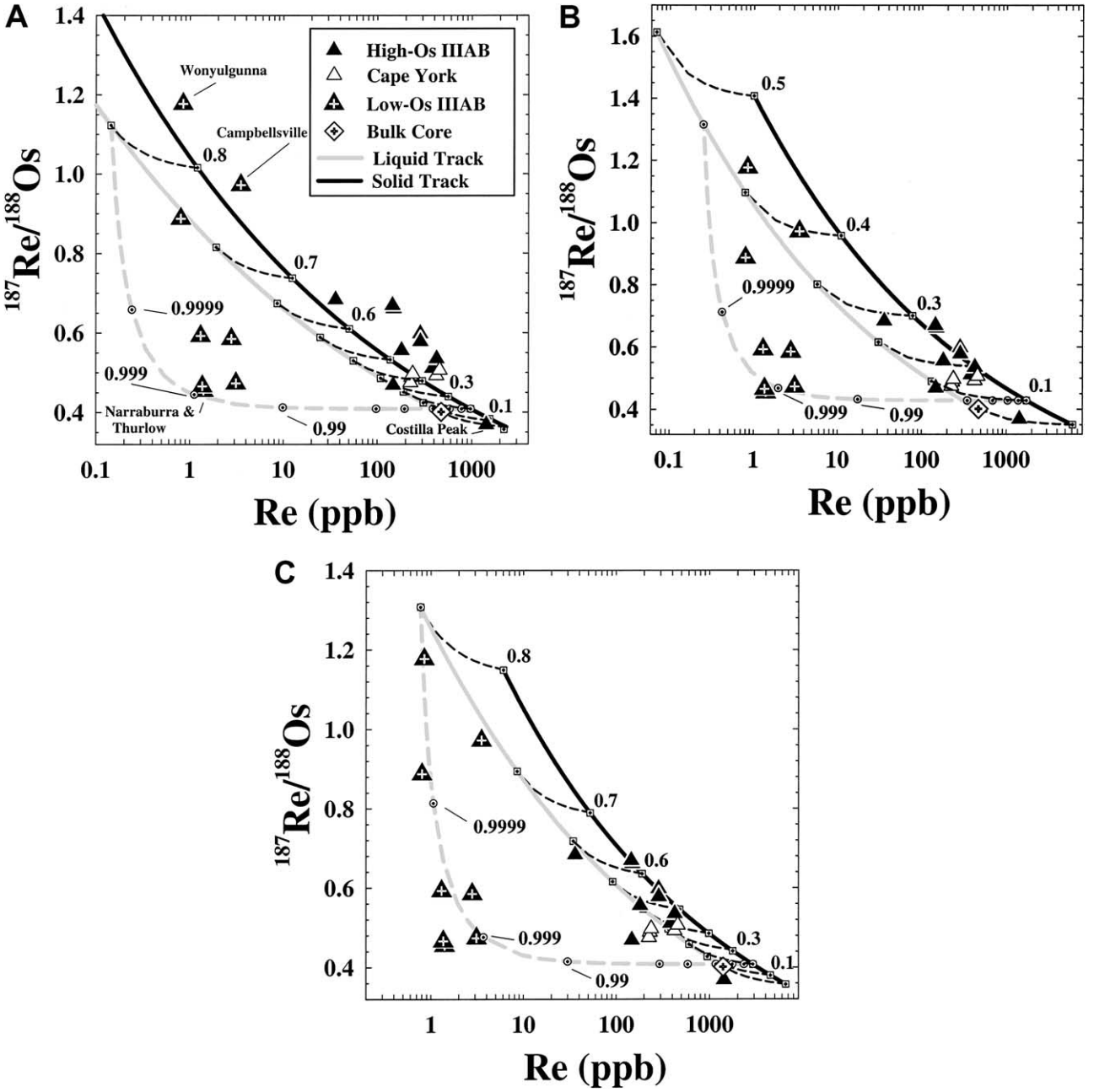

Fig. 6. (a) Rhenium (in ppb) vs. $^{187}Re/^{188}Os$ evolution and mixing diagram. Model 1 from text. Note that the Re axis is logarithmic. Solid and liquid tracks for fractional crystallization of the IIIAB iron system were calculated with D_{Re} and D_{Os} values varying from 5.0 to 8.3 and 5.5 to 9.2, respectively. The variations in D are consistent with 0–80% fractional crystallization of a system with S ranging from 20 to 99 mg/g and P ranging from 4.8 to 20 mg/g, comparable to the model of Wasson (1999). The bulk core is defined as: Re = 470 ppb; Os = 5650 ppb; and a chondritic $^{187}Re/^{188}Os = 0.40$. Small open squares on liquid and solid tracks indicate the fraction of crystal–liquid fractionation (e.g., 0.2 = 20% fractional crystallization). Black dashed curves connect equilibrium solids and liquids. A mixing curve (dashed gray curve) consistent with the production of several of the low-Os samples is shown for solid generated by 20% fractional crystallization of the original liquid and an evolved liquid generated by 80% fractional crystallization. Open circles with dotted centers on this curve represent 20% mixing increments, starting at 0% liquid, then 90, 99, 99.9, and 99.99% liquid increments. (b) Model 2 from text. The same parameters as for model 1 were used, except with D_{Re} and D_{Os} values varying from 13.0 to 14.5 and 14.9 to 16.6, respectively, for 0 to 50% fractional crystallization. A mixing curve (dashed gray curve) consistent with the production of several of the low-Os samples is shown for solid generated by 10% fractional crystallization of the original liquid and an evolved liquid generated by 45% fractional crystallization. Open circles with dotted centers on this curve represent 20% mixing increments, starting at 0% liquid, then 90, 99, 99.9, and 99.99% liquid increments. (c) Model 3 from text. The same D values were used as in model 1. The bulk core is defined as: Re =1400 ppb; Os = 16,800 ppb; $^{187}Re/^{188}Os = 0.40$. A mixing curve (dashed gray curve) is shown for solid generated by 20% fractional crystallization of the original liquid and an evolved liquid generated by 80% fractional crystallization. Open circles with dotted centers on this curve represent 20% mixing increments, starting at 0% liquid, then 90, 99, 99.9, and 99.99% liquid increments.

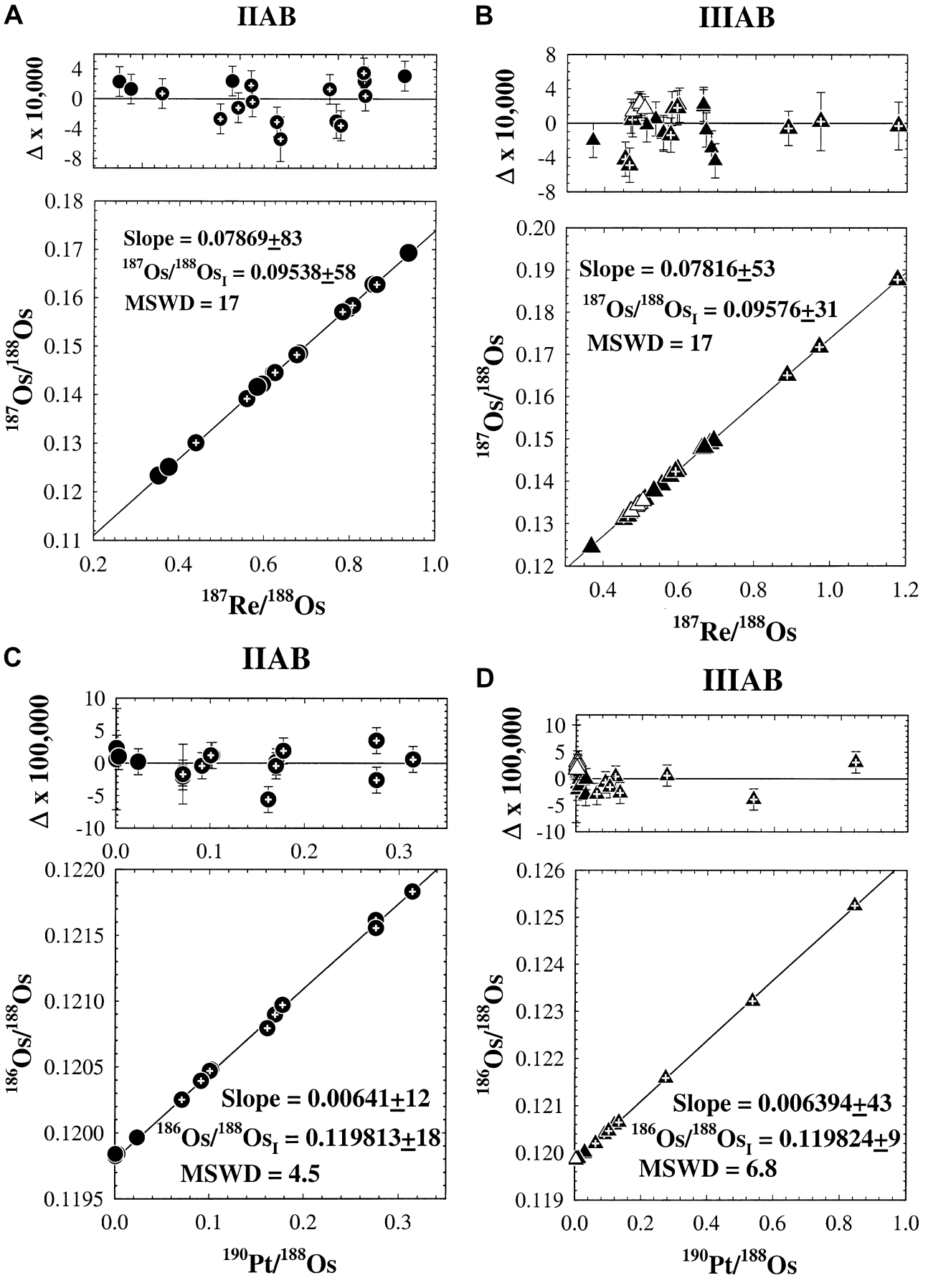
A
IIAB
Δ x 10,000
Slope = 0.07869±83
187Os/188Os_I = 0.09538±58
MSWD = 17
187Os/188Os
187Re/188Os
B
IIIAB
Δ x 10,000
Slope = 0.07816±53
187Os/188Os_I = 0.09576±31
MSWD = 17
187Os/188Os
187Re/188Os
C
IIAB
Δ x 100,000
Slope = 0.00641±12
186Os/188Os_I = 0.119813±18
MSWD = 4.5
186Os/188Os
190Pt/188Os
D
IIIAB
Δ x 100,000
Slope = 0.006394±43
186Os/188Os_I = 0.119824±9
MSWD = 6.8
186Os/188Os
190Pt/188Os

tionates are also missing from the IIIAB suite sampled by the Earth.

In model 3 we use another approach that accounts for the high Re/Os ratios in several of the high-Os irons as mixtures of equilibrium solids and liquids. Model 1 was modified by changing the starting composition of the bulk core. If a bulk core is defined as: Re = 1400 ppb; Os = 16,800 ppb; and $^{187}Re/^{188}Os$ = 0.40, the liquid and solid tracks of model 1 are simply shifted to the right on the plot of Re vs. Re/Os (Fig. 6c). Such a shift allows a good match of the solid track to the data trend for the high-Os irons that have the highest Re/Os ratios. For this model, most of the high-Os IIIAB irons plot between the solid and liquid tracks and can be explained as mixes of equilibrium solids and liquids with 30% to 60% fractional crystallization (process 1). As with the simple version of model 1, the low-Os irons must be generated via the mixing of highly evolved liquids and early-formed solids, although the samples with the lowest Re/Os ratios (Thurlow and Narraburra) would require liquids generated by more than 85% fractional crystallization.

Several aspects of this third model, however, are problematic. First, Costilla Peak has a substantially lower Re/Os ratio than any compositions permitted by solid–liquid mixing. Second, the initial solids generated by this model are far more enriched in Re and Os than any known IIIAB iron (approx. 6600 ppb Re vs. 2190 ppb for the most enriched IIIAB iron, Picacho). This implies that a large fraction of the early-crystallized IIIAB core was not sampled by Earth. A related third problem is that the assumed starting Re and Os concentrations are much higher than are expected for bulk cores, and are also significantly higher than those reported in chondritic metals (Luck et al., 1980). The inferred initial Re/Au and Os/Au ratios would be ≥2× higher than those in known chondrites (other than the so-called CH chondrites, which may not be of nebular origin: e.g., Wasson and Kallemeyn, 1990).

In summary, there are problems with each of the models. We therefore offer no preferred model. The predicted initial solids for model 1 best match the average data, but it is only possible to account for the majority of IIIAB data between the solid and liquid tracks if sampling errors are large, ≥6%, or if the initial Re/Os ratio were ~20% higher than the mean chondritic ratio. Model 2 appears to best fit the majority of the data but requires high D values that may be inconsistent with the concentrations of other trace elements; it also predicts that substantial initial and final fractions of IIIAB are unsampled by Earth. Model 3 requires much higher initial metal concentrations of Re and Os than may be likely for a chondritic precursor. If sampling errors are ≤6%, all models require ubiquitous contamination of late melts by early-crystallized solids to generate the low-Os irons with low Re/Os. This may require physically implausible circumstances such as closely spaced (closer than 1 m) veins permeating most of the core. The failures of the three models suggest that: (a) sampling errors are large, ≥6%, (b) the models do not sufficiently reflect the processes involved, (c) the parameters used in the models are incorrect, (d) the IIIAB samples examined are not sufficiently representative of the core sampled, or (e) a combination of a–d.

Table 3. Regression results for Re-Os isotopic systematics. The errors in the initial $^{187}Os/^{188}Os$ ratios and in the slopes are 2σ. The errors in the ages reflect only the uncertainties in the slopes of the isochrons and do not include the uncertainty in the decay constant for ^{187}Re.

Group	Initial	Slope	Age (Ma)	MSWD
High-Os IIAB	0.09549 (35)	0.07889 (70)	4558 ± 39	2.6
Low-Os IIAB	0.09503 (94)	0.0791 (13)	4569 ± 73	14
IIAB (all)	0.09538 (58)	0.07869 (83)	4546 ± 46	17
High-Os IIIAB	0.09591 (57)	0.0780 (10)	4506 ± 56	12
Low-Os IIIAB	0.09554 (59)	0.07837 (82)	4529 ± 46	24
IIIAB (all)	0.09576 (31)	0.07816 (51)	4517 ± 28	17
Cape York	0.0952 (11)	0.0793 (23)	4579 ± 130	0.9

5.3. Chronology

Rhenium-Os and Pt-Os isotopic data for IIAB and IIIAB irons were separately regressed using Isoplot/Ex (Ludwig, 1999) (Fig. 7a–d). Regression results are summarized in Tables 3 and 4. Each isochron diagram includes a companion graph showing the deviation in $^{187}Os/^{188}Os$ (in the fourth significant figure), or $^{186}Os/^{188}Os$ (in the fifth significant figure) defined as Δ, for each datum relative to the appropriate composite group isochron (IIAB or IIIAB). Associated analytical uncertainties (2σ) in units for composite isotopic compositions and parent-daughter ratios also are provided. Δ values were calculated using the following equations:

$$\text{Re-Os: } \Delta = {}^{187}Os/^{188}Os_{measured} - (S \times {}^{187}Re/^{188}Os) - {}^{187}Os/^{188}Os_{initial}$$

$$\text{Pt-Os: } \Delta = {}^{186}Os/^{188}Os_{measured} - (S \times {}^{190}Pt/^{188}Os) - {}^{186}Os/^{188}Os_{initial}$$

where S denotes the slope of the reference isochron, and $^{187}Os/^{188}Os_{initial}$ and $^{186}Os/^{188}Os_{initial}$ are the initial ratios of the reference isochrons. Individual Δ values for each sample are listed in Tables 1 and 2.

5.3.1. *^{187}Re-^{187}Os System*

The high-Os IIAB Re-Os isochron results reported here agree within uncertainties of those reported by Horan et al. (1992), Morgan et al. (1995), and the higher precision results of Shen et al. (1996) and Smoliar et al. (1996) (Table 5). The higher uncertainties here relative to the latter two studies may result from the limited number of high-Os irons analyzed in this

Fig. 7. (a) $^{187}Re/^{188}Os$ vs. $^{187}Os/^{188}Os$ for group IIAB iron meteorites. Δ values are calculated relative to the IIAB isochron. See text for explanation of Δ. Error bars (2σ) represent the total analytical uncertainty resulting from the isotopic measurements and the blank corrections. (b) $^{187}Re/^{188}Os$ vs. $^{187}Os/^{188}Os$ for group IIIAB iron meteorites. Δ values are calculated relative to the IIIAB isochron. (c) $^{190}Pt/^{188}Os$ vs. $^{186}Os/^{188}Os$ for group IIAB iron meteorites. Δ values are calculated relative to the IIAB isochron. (d) $^{190}Pt/^{188}Os$ vs. $^{186}Os/^{188}Os$ for group IIIAB iron meteorites. Δ values are calculated relative to the IIIAB isochron.

Table 4. Pt-Os isochron regression results. The errors in the initial $^{186}Os/^{188}Os$ ratios and in the slopes are 2σ. The errors in the ages reflect only the uncertainties in the slopes of the isochrons and do not include the uncertainty in the decay constant for ^{190}Pt.

Group	Initial	Slope	Age (Ma)	MSWD
High-Os IIAB	0.119827 (23)	0.00593 (19)	4006 ± 1300	2.0
Low-Os IIAB	0.119798 (31)	0.00648 (18)	4374 ± 120	4.5
IIAB (all)	0.119813 (18)	0.00641 (12)	4323 ± 80	4.5
High-Os IIIAB	0.119835 (11)	0.00562 (94)	3793 ± 630	5.9
Low-Os IIIAB	0.119804 (28)	0.006432 (73)	4341 ± 49	3.6
IIIAB (all)	0.119824 (9)	0.006394 (43)	4315 ± 29	6.8

study (4). The low-Os IIAB irons and combined high- and low-Os IIAB isochron also are identical within uncertainties of the Shen et al. (1996) and Smoliar et al. (1996) results for high-Os IIAB irons. Thus, as with Morgan et al. (1995), no age differences between high- and low-Os IIAB irons can be resolved using the Re-Os system. As with all the new Re-Os and Pt-Os isochrons reported here, Mean Square Weighted Deviation (MSWD) values are significantly higher than 1 and require either minor open-system behavior, or minor underestimation of analytical uncertainties.

The high-Os IIIAB isochron results reported here agree within uncertainties of the isochron results for high-Os IIIAB irons reported by Smoliar et al. (1996), as do the results for the low-Os and the combined high- and low-Os IIIAB data. The only high-precision data to which the composite IIIAB results can be compared are those compiled from Shen et al. (1996) and Chen et al. (2002) (Table 5). Both of the cited studies were conducted in the same laboratory (Caltech) using similar techniques. The results are in generally good agreement, although the precision of the composite isochron generated from Shen et al. (1996) and Chen et al. (2002) suffers from the limited number of high-Os irons analyzed (2). Similar to the IIAB system, we conclude that there is no resolvable age difference between the Re-Os ages of the high-Os and low-Os IIIAB irons. The results imply that any age difference between the high- and low-Os subgroups of either system is less than 40–50 Ma. This conclusion is supported by the systematics of several short-lived chronometers that also suggest metal segregated from silicate and crystallized within short intervals of time for various groups of iron meteorites, including IIAB and IIIAB irons. The Pd-Ag and Hf-W systematics of IIAB and IIIAB irons suggest that their parent bodies formed within several Ma of each other (Chen and Wasserburg, 1996; Harper and Jacobsen, 1996; Lee and Halliday, 1996; Horan et al., 1998; Carlson and Hauri, 2001; Chen et al., 2002). The presence of radiogenic ^{107}Ag, produced by the short-lived parent ^{107}Pd ($t_{1/2}$ = 9.4 Ma), in the IIAB and IIIAB iron meteorites requires rapid accretion and differentiation of the IIAB and IIIAB parent bodies (Chen and Wasserburg, 1996). Additionally, radiogenic ^{53}Cr produced by the short-lived parent ^{53}Mn ($t_{1/2}$ = 3.7 Ma) has been detected in phosphates found in eight IIIAB irons (Hutcheon and Olsen, 1991; Hutcheon et al., 1992). These data indicate a formation interval of approximately 15 Ma for these IIIAB irons. All three short-lived chronometers indicate that the IIAB and IIIAB irons crystallized nearly simultaneously and that the formation interval likely lasted 15 Ma or less. Thus, the Re-Os data from this study for the IIAB and IIIAB irons are consistent with the data from the short-lived chronometers.

The crystallization age of the Cape York suite is of particular interest because the composition trends for this suite indicate the involvement of derivative crystal–liquid fractionation processes (see above). The moderate spread in Re/Os ratio for this suite permits the assessment of a Re-Os crystallization age, albeit a relatively imprecise age (Table 3). The age of 4579 ± 130 Ma and initial ratio of 0.0952 ± 0.0011 are indistinguishable, within uncertainties, from the high-Os IIIAB iron isochron (that includes the Cape York suite) and the combined high-Os and low-Os IIIAB isochron. Although not a precise constraint on the crystallization age of this suite, the results indicate crystallization and subsequent closed-system behavior within 150 Ma of the origin of the solar system.

5.3.2. *^{190}Pt-^{186}Os System*

The Pt-Os isochron data from this study for IIAB irons are in good agreement with the less precise results reported by Walker et al. (1997). Both slope and intercept are within the

Table 5. Comparison of Re-Os results for iron meteorites determined by negative thermal ionization mass spectrometry. For consistency of comparisons, all regressions were recalculated using ISOPLOT (Ludwig, 1999) and the uncertainties cited for each publication (2σ). Groups and subgroup divisions are provided as per source. Results from this study are in boldface.

Group	Reference	Initial	Slope	Age (Ma)	MSWD
IIA	Horan et al. (1992)	0.09595 (45)	0.07824 (68)	4522 ± 38	2.4
IIA	Morgan et al. (1995)	0.09609 (49)	0.07804 (76)	4510 ± 42	7.5
IIA	Smoliar et al. (1996)	0.09543 (8)	0.07852 (2)	4537 ± 8	1.1
IIA	Shen et al. (1996)	0.09563 (12)	0.07848 (20)	4535 ± 11	3.5
IIA	Birck and Allègre (1998)	0.09556 (99)	0.0789 (13)	4561 ± 73	56
High-Os IIAB	**This study**	**0.09549 (35)**	**0.07889 (70)**	**4558 ± 39**	**2.6**
IIB	Morgan et al. (1995)	0.0957 (22)	0.0794 (36)	4584 ± 200	11
Low-Os IIAB	**This study**	**0.09503 (94)**	**0.0791 (13)**	**4569 ± 73**	**14**
IIAB	Morgan et al. (1995)	0.0961 (10)	0.0784 (16)	4533 ± 91	13
IIAB (all)	**This study**	**0.09538 (58)**	**0.07869 (83)**	**4546 ± 46**	**17**
IIIA	Smoliar et al. (1996)	0.09524 (7)	0.07887 (22)	4558 ± 12	1.5
High-Os IIIAB	**This study**	**0.09591 (57)**	**0.0780 (10)**	**4506 ± 56**	**12**
IIIAB	Shen et al. (1996) + Chen et al. (2002)*	0.0946 (42)	0.0802 (75)	4629 ± 420	26
IIIAB (all)	**This study**	**0.09576 (31)**	**0.07816 (51)**	**4517 ± 28**	**17**

* Results for IIIA and IIIB irons were combined from Shen et al. (1996) and Chen et al. (2002) for IIIAB isochron.

uncertainties reported by that study, although the IIAB isochron of this study is much more precise. This is the first study to report Pt-Os isochron data for IIIAB irons. The initial $^{186}Os/^{188}Os$ ratios for both IIAB and IIIAB irons obtained from their respective isochrons agree within uncertainty of the predicted solar system initial $^{186}Os/^{188}Os$ ratio of 0.119820 calculated by Walker et al. (1997) from present day chondritic $^{186}Os/^{188}Os$ and Pt/Os.

The Pt-Os data from this study do not reveal within-group age differences for either IIAB or IIIAB irons. The ages of the high- and low-Os IIAB irons are not resolvable within uncertainty, nor are the ages of the high- and low-Os IIIAB irons (Table 4). It is important to note, however, that because of the limited variations in Pt/Os within the high-Os subgroups, the uncertainties for the Pt-Os ages are very large. In addition, the Pt-Os data from this study do not reveal resolvable age differences between the two iron groups. The regression slopes for both groups differ by only 2.5%.

The IIAB and IIIAB Pt-Os ages of 4323 ± 80 and 4315 ±29 Ma (Table 4) were calculated using a decay constant for ^{190}Pt with a value of 1.477×10^{-12} a^{-1} (Begemann et al., 2001). Thus, the calculated Pt-Os ages are approximately 230 Ma younger than the corresponding Re-Os ages and do not overlap within uncertainties. This difference can be interpreted in one of at least two ways: 1) given that the slopes of the Pt-Os isochrons are dominated by the most highly fractionated irons of each group, the apparent age differences may reflect true age differences between early and late fractionates, or 2) the ^{190}Pt decay constant used in determining the age is too high and requires additional revision.

To address the first possibility, it is important to assess whether it is physically plausible for core metal to remain molten in an asteroidal core for approximately 200 Ma. Due to its high thermal conductivity, the metallic core of a parent body behaves essentially isothermally. Thus, the outer silicate layers control the cooling of the entire parent body. Previous studies have argued that regolith could substantially prolong the cooling of an iron core (e.g., Haack et al., 1990). This explanation, however, cannot account for the discrepancy between the Re-Os and Pt-Os ages. If portions of the IIAB and IIIAB cores remained molten for circa 200 Ma, the within-group Re-Os age differences should also reflect such prolonged cooling and crystallization. Age differences of this magnitude would be resolvable at the current level of uncertainty. The within-group Re-Os ages suggest that the IIAB and the IIIAB parent body cores crystallized over a period of a few tens of millions of years, not hundreds of Ma. Thus, the Re-Os data are inconsistent with the differences in the Pt-Os ages having resulted from core crystallization durations on the order of several hundred Ma.

The discrepancy between the two systems is most likely due to inaccurate Pt-Os ages resulting from an incorrect determination of the decay constant for ^{190}Pt. Various factors hamper the direct determination of decay constants for long-lived alpha emitters, such as ^{190}Pt, via counting methods. For example, the low specific activities require large, uniform sources. Also, although shielding can reduce external background, internal background may result from radioactive alpha contaminants in impure source and counter materials (Al-Bataina and Jänecke, 1987).

Direct determinations of the decay constant for ^{190}Pt have been made by MacFarlane and Kohman (1961), Petrzhak and Yakunin (1962), Graeffe (1963), and Al-Bataina and Jänecke (1987) and have values of 1.005×10^{-12} a^{-1} ± 7.2%, 1.475×10^{-12} a^{-1} ± 36%, 1.284×10^{-12} a^{-1} ± 11%, and 1.042×10^{-12} a^{-1} ± 4.2%, respectively. Al-Bataina and Jänecke (1987) also reported a weighted average for the decay constant, based on all four studies, with a value of 1.066×10^{-12} a^{-1} ± 3.4%. Only the value determined by Petrzhak and Yakunin (1962) is similar to the value chosen by Begemann et al. (2001). The values for the decay constant from the other three studies are substantially lower than the value of Petrzhak and Yakunin. These three decay constants applied to the Pt-Os data from this study yield ages for the IIAB and IIIAB irons that far exceed (>400 Ma) the accepted age of the solar system (4.56 Ga). Clearly, none of these decay constants produces Pt-Os ages that agree with the Re-Os ages. The wide variation in values for the decay constant obtained via counting methods illustrates the difficulties encountered in this approach. Until direct measurements furnish reproducible results, determining a value for the decay constant via geological comparison appears to be a better approach.

The geological comparison method, however, has also proven problematic. The ^{190}Pt decay constant reported by Walker et al. (1997) and subsequently revised by Begemann et al. (2001) were generated via the geological comparison method. In brief, the Pt-Os isotopic systematics of sulfide-bearing ores from the Noril'sk mining district, Russia, were examined. The suite of samples examined had $^{190}Pt/^{188}Os$ ratios that varied by 5 orders of magnitude. A regression of these data resulted in an isochron with a well-defined slope of 0.0003875 ± 32. A precise and accurate age of 251.2 ± 0.3 Ma for the Noril'sk ore host rock had previously been determined via the U-Pb method (Kamo et al., 1996). Combining the U-Pb age for the Noril'sk system with the slope of the isochron and the atomic percentage of ^{190}Pt defined a decay constant with a value of 1.542×10^{-12} a^{-1} ± 1%. Walker et al. (1997) used an atomic percentage of 0.0124% for ^{190}Pt in calculating the value for the decay constant. Morgan et al. (2002) redetermined the atomic percentage of ^{190}Pt to be 0.01296% using multi-collector ICP-MS. The revised atomic percentage shifts the value for the decay constant reported by Walker et al. (1997) to the value reported by Begemann et al. (2001) and used in this study (1.477×10^{-12} a^{-1} ± 1%). Walker et al. (1997), however, used less refined mass spectrometric techniques (via quadrupole ICP-MS) to determine Pt abundances. Consequently, the two data sets may not be quite comparable.

Pending future work, the Re-Os and Pt-Os data obtained in this study provide a means for estimating a value for the ^{190}Pt decay constant. To calculate the decay constant, two assumptions must be made: the Re-Os and Pt-Os ages are equal with regard to the IIAB and IIIAB iron meteorites, and the Re-Os ages are correct. Combining the slope from the Pt-Os isochron for the IIAB irons with the age from the Re-Os isochron yields a value of 1.408×10^{-12} a^{-1} with an uncertainty of ±2.2%. Repeating this procedure using the isochron parameters for the Pt-Os slope and Re-Os age for the IIIAB irons yields a value of 1.415×10^{-12} a^{-1} with an uncertainty of ± 0.9%. In both cases, the uncertainty takes into account both the uncertainty in the slope of the Pt-Os isochron and in the Re-Os age. Both

values for the decay constant agree within the uncertainties. Of these two values, the decay constant defined by the IIIAB irons is preferable due to its smaller uncertainty.

6. CONCLUSIONS

The Pt-Re-Os elemental systematics of the IIAB and IIIAB irons are dominated by the effects of fractional crystallization. For the IIAB irons, solid metal–liquid metal bulk distribution coefficients (D values) are $D_{Os}>D_{Re}>>D_{Pt}>1$ during the initial stages of core crystallization. As has been previously noted, there is a major change in D_{Re}/D_{Os} approximately at the structural divide between hexahedrites and octahedrites. The latter stages of IIAB crystallization are characterized by D values for Pt>Re>Os. This is reflected in the increasing Re/Os ratio during crystallization of hexahedrites, and the decreasing ratio during crystallization of octahedrites.

The relative partitioning behaviors of these elements are much more complex in the IIIAB irons relative to the IIAB irons, mainly a reflection of mixing of solid metal and either trapped equilibrium melts or more evolved melts. As with the IIAB irons, solid metal–liquid metal D values for the initial stages of IIIAB core crystallization show $D_{Os}>D_{Re}>>D_{Pt}>1$. Because of the scatter in the data, it is currently impossible to estimate relative values for D_{Pt}-D_{Re}-D_{Os} in the low-Os IIIAB irons. Part of the scatter may result from the partitioning of Re or Os into phases that were not present in representative amounts in our samples. The partitioning behaviors of Pt, Re, and Os into minor phases will require further study to test this hypothesis.

The Re-Os data for IIAB and IIIAB irons define isochrons corresponding to ages of 4530 ± 50 Ma and 4517 ± 32 Ma, respectively. These results agree within uncertainty with those of previous studies (Shen et al., 1996; Smoliar et al., 1996). The relatively large error in the Re-Os age for high-Os IIAB irons is likely due to the small sample size. The Re-Os data do not reveal within-group or between-group differences with respect to the onset of core crystallization.

The Pt-Os data for IIAB and IIIAB irons define isochrons corresponding to ages of 4323 ± 80 Ma and 4325 ±26 Ma, respectively. The results for the IIAB irons agree within uncertainty with those of Walker et al. (1997). Both isochrons are well-defined, and the uncertainty for the IIAB irons has been reduced by a factor of approximately 3.5 relative to Walker et al. (1997). The Pt-Os data do not reveal within-group or between-group differences with respect to the onset of core crystallization.

The Re-Os and Pt-Os ages do not agree within uncertainty for either the IIAB or IIIAB irons. This discrepancy most likely stems from an incorrect decay constant for ^{190}Pt. Previously published values differ by as much as a factor of 1.5. A new value of 1.415×10^{-12} a^{-1}, based on the Pt-Os slope and Re-Os age for the IIIAB irons, is tentatively recommended.

Acknowledgments—This work was partially supported by NSF CSEDI grant 0001921 (to R.J.W.), and NASA Cosmochemistry grants NAGW 3625 and NAG 54769 (to R.J.W.) and NAGW 5-12887 (to J.T.W.). Samples were obtained from the Smithsonian Institution's National Museum of Natural History, and the Geological Museum, University of Copenhagen. Provision of these materials is greatly appreciated. We especially thank Roy Clarke for his long-term assistance on this project. We thank Michael Smoliar for Figure 5a–c, which originally appeared in Smoliar (1996). We thank J.-L. Birck, S. B. Jacobsen, and J. H. Jones for thorough reviews, and also Associate Editor G. Herzog for his insightful comments.

Associate editor: G. Herzog

REFERENCES

Al-Bataina B. and Jänecke J. (1987) Half-lives of long-lived alpha emitters. *Radiochim. Acta* **42,** 159–164.

Becker H., Walker R. J., MacPherson G. J., Morgan J. W., and Grossman J. N. (2001) Rhenium-osmium systematics of calcium-aluminum-rich inclusions in carbonaceous chondrites. *Geochim. Cosmochim. Acta* **65,** 3379–3390.

Begemann F., Ludwig K. R., Lugmair G. W., Min K., Nyquist L. E., Patchett P. J., Renne P. R., Shih C.-Y., Villa I. M., and Walker R. J. (2001) Call for an improved set of decay constants for geochronological use. *Geochim. Cosmochim. Acta* **65,** 111–121.

Birck J.-L. and Allègre C.-J. (1998) Rhenium-187-osmium-187 in iron meteorites and the strange origin of the Kodaïkanal meteorite. *Meteoritics & Planet. Sci.* **33,** 647–653.

Brandon A. D., Snow J. E., Walker R. J., Morgan J. W., and Mock T. D. (2000) ^{190}Pt-^{186}Os and ^{187}Re-^{188}Os systematics of abyssal peridotites. *Earth Planet. Sci. Lett.* **177,** 319–335.

Buchwald V. F. (1975) *Handbook of Iron Meteorites,* Vol. 1. University of California Press, Berkeley, CA, 243 pp.

Carlson R. W. and Hauri E. H. (2001) Extending the ^{107}Pd-^{107}Ag chronometer to low Pd/Ag meteorites with multicollector plasma-ionization mass spectrometry. *Geochim. Cosmochim. Acta* **65,** 1839–1848.

Chabot N. L. and Drake M. J. (1999) Crystallization of magmatic iron meteorites. The role of mixing in the molten core. *Meteorit. Planet. Sci.* **34,** 235–246.

Chabot N. L., Campbell A. J., Jones J. H., Humayun M., and Agee C. B. (2003) Applying experimental partitioning results to iron meteorites: A test of Henry's law. *Meteorit. Planet. Sci.* **38,** 181–196.

Chen J. H., Papanastassiou D. A., and Wasserburg G. J. (2002) Re-Os and Pd-Ag systematics in Group IIIAB irons and in pallasites. *Geochim. Cosmochim. Acta* **66,** 3793–3810.

Chen J. H. and Wasserburg G. J. (1996) Live ^{107}Pd in the early solar system and implications for planetary evolution. *Geophys. Monogr. Ser.* **95,** 1–20 AGU.

Choi B.-G., Ouyang X., and Wasson J. T. (1995) Classification and origin of IAB and IIICD iron meteorites. *Geochim. Cosmochim. Acta* **59,** 593–612.

Clayton R. N. and Mayeda T. K. (1996) Oxygen isotope studies of achondrites. *Geochim. Cosmochim. Acta* **60,** 1999–2017.

Cohen A. S. and Waters F. G. (1996) Separation of osmium from geological materials by solvent extraction for analysis by thermal ionisation mass spectrometry. *Anal. Chim. Acta* **332,** 269–275.

Esbensen K. H., Buchwald V. F., Malvin D. J., and Wasson J. T. (1982) Systematic compositional variations in the Cape York iron meteorites. *Geochim. Cosmochim. Acta* **46,** 1913–1920.

Graeffe G. (1963) On the alpha activity of platinum isotopes. *Ann. Acad. Sci. Fenn.* **AVI,** 1–14.

Haack H., Rasmussen K. L., and Warren P. H. (1990) Effects of regolith/megaregolith insulation on the cooling histories of differentiated asteroids. *J. Geophys. Res.* **95,** 5111–5124.

Haack H. and Scott E. R. D. (1992) Asteroid core crystallization by inward dendritic growth. *J. Geophys. Res.* **97,** 14,727–14,734.

Haack H. and Scott E. R. D. (1993) Chemical fractionations in group IIIAB iron meteorites: Origin by dendritic crystallization of an asteroidal core. *Geochim. Cosmochim. Acta* **57,** 3457–3472.

Harper C. L. and Jacobsen S. B. (1996) Evidence for ^{182}Hf in the early solar system and constraints on the timescale of terrestrial accretion and core formation. *Geochim. Cosmochim. Acta* **60,** 1131–1153.

Hirt B., Herr W., Hoffmeister W. (1963) Age determinations by the rhenium-osmium method. In *Radiometric Dating.* International Atomic Energy Agency, Vienna, pp. 35–43.

Horan M. F., Morgan J. W., Walker R. J., and Grossman J. N. (1992) Re-Os isotope constraints on the age of iron meteorites. *Science* **255,** 1118–1121.

Horan M. F., Smoliar M. I., and Walker R. J. (1998) ^{182}W and ^{187}Re-^{187}Os systematics of iron meteorites: Chronology for melting, differentiation and crystallization in asteroids. *Geochim. Cosmochim. Acta* **62,** 545–554.

Horan M. F., Walker R. J., Morgan J. W., Grossman J. N. and Rubin A. (2003) Highly siderophile elements in chondrites. *Chem. Geol.* **196,** 5–20.

Hutcheon I. D. and Olsen E. (1991) Cr isotopic composition of differentiated meteorites: A search for ^{53}Mn (abstract). *Lunar Planet. Sci.* **XXII,** 605–606.

Hutcheon I. D., Olsen E., Zipfel J., and Wasserburg G. J. (1992) Cr isotopes in differentiated meteorites: Evidence for ^{53}Mn. *Lunar Planet. Sci.* **XXIII,** 565–566.

Jones J. H. and Drake M. J. (1983) Experimental investigation of trace element fractionation in iron meteorites, II: The influence of sulfur. *Geochim. Cosmochim. Acta* **47,** 1199–1209.

Jones J. H. and Malvin D. J. (1990) A nonmetal interaction model for the segregation of the trace metals during solidification of Fe-Ni-S, Fe-Ni-P, Fe-Ni-S-P alloys. *Metall. Trans. B* **21B,** 697–706.

Jones J. H. (1994) Fractional crystallization of iron meteorites: Constant *vs.* changing partition coefficients. *Meteoritics* **29,** 423–426.

Jones J. H. (1995) Reply to comment by J. W. Morgan. *Meteoritics* **30,** 354–356.

Kamo S. L., Czamanske G. K., and Krogh T. E. (1996) A minimum U-Pb age for Siberian flood-basalt volcanism. *Geochim. Cosmochim. Acta* **60,** 3505–3511.

Kelly W. R. and Larimer J. W. (1977) Chemical fractionations in meteorites-VIII. Iron meteorites and the cosmochemical history of the metal phase. *Geochim. Cosmochim. Acta* **41,** 93–111.

Lee D.-C. and Halliday A. N. (1996) Hf-W isotope evidence for rapid accretion and differentiation in the early solar system. *Science* **274,** 1876–1879.

Luck J.-M., Birck J. L., and Allègre C. J. (1980) ^{187}Re-^{187}Os systematics in meteorites: Early chronology of the solar system and age of the galaxy. *Nature* **283,** 256–259.

Ludwig K. R. (1999) *User's Manual for Isoplot/Ex*. Berkeley Geochronology Center Special Publication No. 1a, Berkeley, CA, 49 pp.

MacFarlane R. D. and Kohman T. P. (1961) Natural alpha radioactivity in medium-heavy elements. *Phys. Rev.* **121,** 1758–1769.

Morgan J. W., Walker R. J., and Grossman J. N. (1992) Rhenium-osmium isotope systematics in meteorites I: Magmatic iron meteorite groups IIAB and IIIAB. *Earth Planet. Sci. Lett.* **108,** 191–202.

Morgan J. W. (1995) Comment on "Fractional crystallization of iron meteorites: constant *vs.* changing partition coefficients" by J. H. Jones. *Meteoritics* **30,** 352–353.

Morgan J. W., Horan M. F., Walker R. J., and Grossman J. N. (1995) Rhenium-Osmium concentration and isotope systematics in group IIAB iron meteorites. *Geochim. Cosmochim. Acta* **59,** 2331–2344.

Morgan J. W., Walker R. J., Horan M. F., and Beary E. S. (2002) ^{190}Pt-^{186}Os and ^{187}Re-^{187}Os systematics of the Sudbury Igneous Complex, Ontario. *Geochim. Cosmochim. Acta* **66,** 273–290.

Narayan C. and Goldstein J. I. (1982) A dendritic crystallization model to explain Ge-Ni variations in iron meteorites. *Geochim. Cosmochim. Acta* **46,** 259–268.

Pernicka E. and Wasson J. T. (1987) Ru, Re, Os, Pt, and Au in iron meteorites. *Geochim. Cosmochim. Acta* **51,** 1717–1726.

Petrzhak K. A. and Yakunin M. I. (1962) Investigation of the alpha radioactivity of natural platinum. *Sov. Phys. JETP* **14,** 1256–1266.

Roy-Barman M. and Allègre C. J. (1994) $^{187}Os/^{186}Os$ ratios of mid-ocean ridge basalts and abyssal peridotites. *Geochim. Cosmochim. Acta* **58,** 5043–5054.

Schoenberg R., Kamber B. S., Collerson K. D., and Eugster O. (2002) New W-isotope evidence for rapid terrestrial accretion and very early core formation. *Geochim. Cosmochim. Acta* **66,** 3151–3160.

Scott E. R. D. (1972) Chemical fractionation in iron meteorites and its interpretation. *Geochim. Cosmochim. Acta* **36,** 1205–1236.

Scott E. R. D. (1977) Geochemical relationship between some pallasites and iron meteorites. *Mineral. Mag.* **41,** 265–272.

Shen J. J., Papanastassiou D. A., and Wasserburg G. J. (1996) Precise Re-Os determinations and systematics of iron meteorites. *Geochim. Cosmochim. Acta* **60,** 2887–2900.

Shirey S. B. and Walker R. J. (1995) Carius tube digestion for low-blank Rhenium-Osmium analyses. *Anal. Chem.* **67,** 2136–2141.

Shirey S. B. and Walker J. W. (1998) The Re-Os isotope system in cosmochemistry and high-temperature geochemistry. *Annu. Rev. Earth Planet. Sci.* **26,** 423–500.

Smoliar M. I., Walker R. J., and Morgan J. W. (1996) Re-Os ages of group IIA, IIIA, IVA, and IVB iron meteorites. *Science* **271,** 1099–1102.

Smoliar M. I (1996) Re-Os isotopic study of magmatic iron meteorites. Ph.D. dissertation, University of Maryland, 105 pp.

Stewart B., Papanastassiou D. A., and Wasserburg G. J. (1996) Sm-Nd systematics of a silicate inclusion in the Caddo IAB iron meteorite. *Earth Planet. Sci. Lett.* **143,** 1–12.

Walker D. (2000) Core participation in mantle geochemistry: Geochemical Society Ingerson Lecture, GSA Denver, October 1999. *Geochim. Cosmochim. Acta* **64,** 2897–2911.

Walker R. J., Morgan J. W., Beary E. S., Smoliar M. I., Czamanske G. K., and Horan M. F. (1997) Applications of the ^{190}Pt-^{186}Os isotope system to geochemistry and cosmochemistry. *Geochim. Cosmochim. Acta* **61,** 4799–4807.

Walker R. J., Horan M. F., Morgan J. W., Becker H., Grossman J. N., and Rubin A. (2002) Comparative ^{187}Re-^{187}Os systematics of chondrites: Implications regarding early solar system processes. *Geochim. Cosmochim. Acta* **66,** 4187–4201.

Wasson J. T. (1974) *Meteorites*. Springer-Verlag, New York, 316 pp.

Wasson J. T. Wang J. M. (1986) A nonmagmatic origin of group-IIE iron meteorites. *Geochim. Cosmochim. Acta* **50,** 725–732.

Wasson J. T. and Kallemeyn G. W. (1990) Allan Hills 85085: A subchondritic meteorite of mixed nebular and regolithic heritage. *Earth Planet. Sci. Lett.* **101,** 148–161.

Wasson J. T. (1999) Trapped melt in IIIAB irons; solid/liquid elemental partitioning during the fractionation of the IIIAB magma. *Geochim. Cosmochim. Acta* **63,** 2875–2889.

Wasson J. T. and Kallemeyn G. W. (2002) The IAB iron-meteorite complex: A group, five subgroups, numerous grouplets, closely related, mainly formed by crystal segregation in rapidly cooling melts. *Geochim. Cosmochim. Acta* **66,** 2445–2473.

Wasson J. T. and Choi B.-G. (2003) Main-group pallasites: Chemical composition, relationship to IIIAB irons, and origin. *Geochim. Cosmochim. Acta* **67,** 3079–3096.

Yin Q. Z., Jacobsen S. B., Lee C.-T., McDonough W. F., Rudnick R. L., and Horn I. (2001) A gravimetric K_2OsCl_6 standard: Application to precise and accurate Os spike calibration. *Geochim. Cosmochim. Acta* **65,** 2113–2127.